Tutor

Dr. Francesc Viñes Solana

Departament de Ciència de Materials i Química Física

Grau de Química

Treball Final de Grau

Compactness and *d*-band filling effect on chemical descriptors for transition metals.

Efecte de la compactació i l'ompliment de la banda *d* en descriptors químics de metalls de transició.

Biel Martínez Díaz

Juny 2017

Universitat de Barcelona

B:KC Barcelona Knowledge Campus
Campus d'Excel·lència Internacional

En el moment d'escriure aquestes línies, em venen al cap records de la etapa que han suposat els quatre darrers anys de la meva vida. Ha estat una etapa plena. Plena d'aprenentatge, d'evolució, de canvis... Es fa difícil centrar els agraïments d'un treball de quatre mesos en el propi treball quan aquest suposa el tancament d'aquests quatre anys, però procuraré que així sigui.

En primer lloc, i no com a formalitat, vull agrair a en Fransis la seva implicació. M'ha descobert una branca de la computacional en la qual mai m'hagués fixat, i m'ha permès gaudir i aprendre un munt. Gràcies.

També he de mencionar els meus companys de despatx. L'Hector i l'Ángel, per estar allà sempre que els he necessitat; en Manel, per les seves classes de matplotlib i de python en general; i en Gerard, per descobrir-me el meravellós món de l'scripting en bash i la feina que estalvia. Gràcies a tots per fer-me sentir tant a gust al despatx, i per ensenyar-me tant.

Agrair també a l'Oriol, per cedir-me el monopoli del cerqt2, sense els seus nodes tot això no hauria sigut possible; i a la Lorena, per el suport moral i per ser una gran aliada en la batalla contra el TPSS, gràcies pels àtoms més rebels.

Per últim, a en Joan. Per aquests quatre mesos però també pels tres anys anteriors. Per compartir alegries i frustracions. Per aguantar les meves xapes i per tot el que he après de tu i el que hem après junts. Seguirem fent camí.

REPORT

CONTENTS

1. SUMMARY

This project bases on the study of the *d*-band center, the width corrected *d*-band center, and the maximum point of the Hilbert transform of the *d*-band as a chemical descriptors for the activity of the hexagonal close packed (*hcp*) transition metal (0001), $(10\bar{1}0)$, and $(11\bar{2}0)$ surfaces. It has been carried out by computational simulations using Density Functional Theroy (*DFT*) with the Perdew-Burke-Ernzerhof (*PBE*) and Tao-Perdew-Staroverov-Scuseria (*TPSS*) approximations for the exchange and correlation functional.

To do so, first, cohesive energies and shortest internuclear distances have been calculated for bulk *hcp*, and compared with previous calculations and experimental data to validate the computational setups. The surfaces have been simulated and some surface properties have been compared with experimental data. These are the fixed surface energy, the relaxed surface energy, and the relaxation energy, as well as the structural surface relaxation. The density of states of each surface has been acquired to obtain estimates of the above commented descriptors.

These values have been examined on their capacity to describe the metallic surfaces activity comparing the results to literature available adsorption energies. The descriptor with best agreement with adsorption energies is the original *d*-band center, as the other two descriptors do not add any additional beneficial information to the *d*-band, given that their trends on adsorption energies are worse.

Keywords: chemical activity descriptors, *d*-band center, transition metals, hexagonal close-packed, surfaces, density functional theory.

2. RESUM

Aquest projecte es basa en l'estudi del centre de la banda *d*, el centre de la banda *d* corregit amb l'amplada, i el punt màxim de la transformada de Hilbert sobre la banda *d,* com a descriptors químics per a la activitat de les superfícies (0001), $(10\bar{1}0)$ i $(11\bar{2}0)$ de tots els metalls de transició que presenten una estructura hexagonal compacta, a partir de simulacions computacionals usant la teoria del funcional de la densitat (*Density Functional Theory - DFT*) amb els funcionals de correlació i intercanvi Perdew-Burke-Ernzerhof (*PBE*) i Tao-Perdew-Staroverov-Scuseria (*TPSS*).

Per dur-ho a terme, s'han calculat primer la energia cohesiva i la distància internuclear més curta pels *bulks* de tots els metalls de transició *hcp* i s'han comparat amb valors obtinguts de càlculs previs i dades experimentals per tal de validar el mètode computacional. Les superfícies s'han simulat, i propietats com la energia superficial fixa, la energia superficial relaxada, i la energia de relaxació, així com la relaxació estructural de la superfície s'han calculat i comparat amb dades experimentals. S'ha obtingut la densitat d'estats de cada superfície per tal d'estimar els descriptors esmentats anteriorment.

Per últim, s'han examinat els valors d'aquests en la seva capacitat de descriure la activitat de les superfícies metàl·liques a partir de càlculs reportats d'energies d'adsorció. S'ha observat que el descriptor que millor es relaciona amb aquestes és el centre de la banda *d*, i que els altres dos no aporten informació addicional beneficiosa a la d'aquest, sinó que descriuen pitjor les tendències observades en les energies d'adsorció.

Paraules clau: descriptors de l'activitat química, centre de la banda *d*, metalls de transició, estructura hexagonal compacta, superfícies, teoria del funcional de la densitat.

3. INTRODUCTION

Since the 1830s, when the catalysis term was firstly introduced in the chemistry knowledge by the chemist Jöns Jacob Berzelius,[1] the physicochemistry of the solid compounds in heterogeneous catalytic processes has been always increasing. Despite that before Berzelius definition catalytic properties had been widely used without identifying the cause, his discoveries opened the doors of an unexplored world with thousands of applications.

The catalytic activity is defined as the capacity of a compound to increase (or modify) the rate of a chemical reaction without being consumed as a reactant. This is achieved through many ways, like by either stabilizing the products or destabilizing the reactants, decreasing the transition state energy barrier between them, by inhibiting side reactions, being resistant to chemical poisons, etc. Cleary, the catalytic activity is complex phenomenon occurring at the atomic level.

Industrial processes are the ones that have been most benefited from the use of catalysts. In fact, is the main sector where catalytic compounds are used. Many of the nowadays most important industrial processes are sustained by the utilization of catalysts, such as the Bosch-Haber process.[2] This process produces ammonia (NH_3) from hydrogen (H_2) and nitrogen (N_2) gases using an Iron catalyst, where this process is of capital importance in the synthesis of fertilizers.

Historically, research on finding and/or improving catalysts has been carried out experimentally, oftentimes driven by chemical intuition. The emergence in the last decades of computational simulations implied an important breakthrough here, because it helped industries in rationally choosing the best catalytic species before the experimental testing, reducing the research costs.[3]

There are many compounds with catalytic properties, but maybe transition metals stand over others as they are of paramount importance in heterogeneous catalysis, typically being the active components in many industrial catalysts, like the above-commented Bosch-Haber process, but also others such as nitric acid synthesis (Ostwald process, catalyst of Pt-Rh),[4] or the hydrogen production by steam process (Nickel catalyst).[5]

The crystallographic structures of the transition metals are shown in Figure 1; there are three predominant patterns: body-centered cubic (*bcc*), face-centered cubic (*fcc*), and hexagonal close-packed (*hcp*). The two firsts are located in a particular part of the periodic table whereas the *hcp* metals are spread out all along. There are two transition metals that do not feature any of those crystal structures; Manganese and Lanthanum. Manganese features a *bcc* arrangement, where crystallographic positions are filled by Mn_{29} clusters instead of atoms. In the case of La, it features a regular hexagonal structure. Finally, Hg is liquid at standard conditions.

hydrogen **H**																	helium **He**
lithium **Li**	beryllium **Be**											boron **B**	carbon **C**	nitrogen **N**	oxygen **O**	fluorine **F**	neon **Ne**
sodium **Na**	magnesium **Mg**											aluminium **Al**	silicon **Si**	phosphorus **P**	sulphur **S**	chlorine **Cl**	argon **Ar**
potassium **K**	calcium **Ca**	scandium **Sc** hcp	titanium **Ti** hcp	vanadium **V** bcc	chromium **Cr** bcc	manganese **Mn** bcc*	iron **Fe** bcc	cobalt **Co** hcp	nickel **Ni** fcc	copper **Cu** fcc	zinc **Zn** hcp	gallium **Ga**	germanium **Ge**	arsenic **As**	selenium **Se**	bromine **Br**	krypton **Kr**
rubidium **Rb**	strontium **Sr**	yttrium **Y** hcp	zirconium **Zr** hcp	niobium **Nb** bcc	molybdenum **Mo** bcc	technetium **Tc** hcp	ruthenium **Ru** hcp	rhodium **Rh** fcc	palladium **Pd** fcc	silver **Ag** fcc	cadmium **Cd** hcp	indium **In**	tin **Sn**	antimony **Sb**	tellurium **Te**	iodine **I**	xenon **Xe**
caesium **Cs**	barium **Ba**	lantanium **La** hex.	hafnium **Hf** hcp	tantalum **Ta** bcc	tungsten **W** bcc	rhenium **Re** hcp	osmium **Os** hcp	iridium **Ir** fcc	platinum **Pt** fcc	gold **Au** fcc	mercury **Hg** liquid	thallium **Tl**	lead **Pb**	bismuth **Bi**	polonium **Po**	astatine **At**	radon **Rn**

Figure 1. Periodic table with most stable crystallographic structures for transition metals.

Computational studies are able to relate most of the catalytic features, like, for instance, the reactant adsorption strength, to particular physicochemical properties of the here treated transition metals. More concretely, and focusing only on *hcp* metals, periodic trends can be explored because of their distribution along the periodic table. These physicochemical properties have been described as chemical descriptors, and their determination for *hcp* transition metals is the main target of this study.

4. OBJECTIVES

The main objective of this project is then to obtain estimates of three commonly proposed chemical descriptors for twelve *hcp* transition metals (Sc, Y, Ti, Zr, Hf, Tc, Re, Ru, Os, Co, Zn, and Cd) by Density Functional Theory (*DFT*) calculations using two different functional approximations, Perdew-Burke-Ernzerhof (PBE)[6] and Tao-Perdew-Staroverov-Scuseria (TPSS)[7], on simulated (0001), $(10\bar{1}0)$, and $(11\bar{2}0)$ surface endings. The *d*-band center, the width corrected *d*-band center, and the maximum point of the Hilbert transform of the *d*-band are the descriptors of interest. In the process of obtaining these descriptors, other properties are calculated, as well as studied on their possible trends or deviations. The detailed objectives of this study are:

- To simulate *hcp* transition metals isolated atoms and bulk structures with both DFT funcionals and estimate their accuracy on the following bulk properties:
    - Cohesive energies.
    - Shortest interatomic distances.
- To model the three surfaces with both functionals for each metal, optimizing their atomic positions, so as to evaluate their performance on describing:
    - Fix and relaxed surface energies, and the relaxation energy.
    - The structural surface relaxation.
- To calculate the density of states for each surface simulation in order to determine the:
    - *d*-band center.
    - Width corrected *d*-band center.
    - Maximum point of the Hilbert transform of the *d*-band.

So, bulk properties will allow checking whether the functionals give coherent results with respect experimental values and also with respect previous calculations, as well as to find out

which functional works better for the metallic systems under study. From the bulk calculations the optimized structures will be used to build the surface structures.

The optimized surface calculations are needed for obtaining afterwards the density of states. Despite there are little studies about surface energies, some of them will also be compared with experimental data and previous calculations, to ascertain their accuracy.

The collection of descriptors will be followed by a study of possible periodic trends, and also by a comparison with previous adsorptive energies trends, which can serve to verify the effectiveness of these descriptors.

5. THEORY

5.1. SOLIDS

Atoms and molecules are called to be in a solid state when they feature a high resistance to volume change or deformations, and they have forces more attractive than liquids. The solid state is one of the four most common states of matter (gas, liquid, solid, and plasma), and it can be divided in two differentiated kinds of solids, amorphous and crystalline solids.

Amorphous solids are characteristic for their non-ordered structure. Atoms or molecules are randomly disordered along the material, as in a static photography of a liquid. Polymeric materials and glass are some examples of amorphous solids. However, crystalline solids feature an atomic ordering typically reflected in their macroscopic structure. In this sense, a basic unit, called unit cell, is periodically repeated all along the material. Every unit cell contains a finite number of atoms or molecules inside in a specific arrangement, so that a large number of repeated cells can be found in a material structure. Unit cells are defined by six quantities, three vectors (cell parameters) and three angles (see Figure 2). The unit cell definition is arbitrary, as there are infinite of them that reproduce the material crystal, although the smallest one that allows the representation of the whole material is called the primitive unit cell.

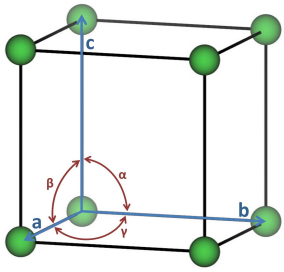

Figure 2. Example of a cubic unit cell with its three vectors (a, b, c) in blue arrows, and three angles (α, β, γ), in red. Green spheres denote atomic positions.

Crystallographic solids can also be classified depending on the origin of their cohesive forces as ionic, molecular, covalent, or metallic solids. The last ones are the ones here treated. Metallic solids can be conceived as cations which stay united because of the interaction with a sea of surrounding electrons. These electrons are free to move around the ionic nuclei, and act

as glue for the system. Given that, the bond is not directional, and the structure of the solids can be simplified to a study of packaging balls with maximum compaction. Taking atoms as spheres, the maximum compaction reachable is a 74% of volume. This occupancy is typically obtained with two different stackings of atomic layers arranged in a planar hexagonal packed display, either ABA or ABC.

Connecting the stacking concept with the unit cell idea, it is possible to define the most usual unit cells for these two stacking patterns: *fcc* and *hcp* cells. The *fcc* has an ABC stacking whereas *hcp* has an ABA stacking.

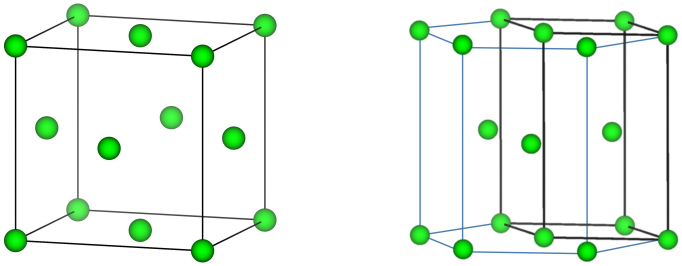

Figure 3. Most common unit cells used in an *fcc* system (left) and in a *hcp* system (right).

5.1.1. Bulk and surface

Bulk is defined as any part of a solid that is surrounded in all directions by the same solid. In other words, is the part of the solid that is inside the structure, only in contact with other parts of the same material. In terms of unit cells, the three dimensional (*3D*) replication of one of those previously defined would simulate a bulk.

In this work there are two bulk properties that shall be calculated. The first one is the shortest interatomic distance, and corresponds to the nearest distance between two atoms in the bulk unit cell. The second one is the cohesive energy, E_{coh}, and gives an idea about the stability of the bulk metal compared to having isolated metal atoms in vacuum.

$$E_{coh} = E_{atom} - \frac{E_{bulk}}{n_{bulk}} \qquad \text{(Eq. 1)},$$

where E_{bulk} is the energy of the unit cell, n_{bulk} the number of atoms in the unit cell, and E_{atom} the energy of an atom isolated in the vacuum.

Surfaces are the parts of a material that are in contact with the media. They can be understood as a cut along a straight plane of the bulk structure, following one of the different infinite possible planes that exist in the material. In order to unequivocally assign these possible planes, Miller indices are defined. Miller indices define the orientation of a surface or a crystal plane by considering where the plane intersects the unit cell axes. The procedure is independent of the packaging pattern of the material, but hexagonal packages have a peculiarity, see below.

Miller indices are expressed as three numbers (i j k), that comes from the inverse of the point each one of the defined space axis are cut. Note that in Miller procedure, this point is expressed in fractional coordinates. The peculiarity of *hcp* Miller indices is that they feature an extra index, l, which is the sum of the two firsts, i and j, with the final sign changed. These new indices (i j l k) are called Miller-Bravais indices. Although a plane is perfectly defined in a 3D lattice with only three indices, a fourth comes useful because forces the axis of the plane to be equal to its normal vector. This comes normal for orthogonal unit cells, but for the *hcp* unit cell this extra index is needed.

Let us now focus on the non-equivalent planes inside the *hcp* structure. In a given unit cell structure, infinite planes can be defined inside. In a bulk structure, atoms tend to be as coordinated as they can, and when a surface is created, that coordination is being broken. The destabilization that the surface atoms suffer is inherently related to the number of atoms that they still have on their surroundings and the ones that are lost. The number of nearest neighbors that an atom has around is defined as the Coordination Number (*CN*). The most stable surfaces should be those with highest CN to cushion the destabilization. This rule-of-a-thumb has been inspected here, as different surfaces have been chosen with high CN, see Figure 4.

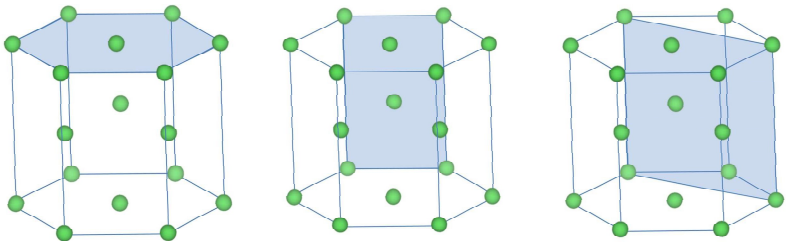

Figure 4. From the left to the right: (0001), $(10\bar{1}0)$, and $(11\bar{2}0)$ *hcp* surfaces.

For each surface, different properties can be calculated: the bulk-truncated (fixed) and relaxed surface energies, the relaxation energy, and the surface structural relaxation. The fixed (γ^{fix}) and relaxed (γ^{relax}) surface energies are calculated as the subtraction between the bulk energy and the slab energy (see below), given per unit of area of the surface ending. Fixed or relaxed surface energies belong to bulk-truncated and relaxed geometries, respectively. The relaxation energy is calculated as the subtraction between the fixed and the relaxed surface energy:

$$\gamma^{\mathrm{fix}} = \frac{\mathrm{E}^{\mathrm{fix}}_{\mathrm{surface}} - \mathrm{N}\,\mathrm{E}_{\mathrm{bulk}}}{2\,\mathrm{A}} \;\mid\; \gamma^{\mathrm{relax}} = \frac{\mathrm{E}^{\mathrm{relax}}_{\mathrm{surface}} - \mathrm{N}\,\mathrm{E}_{\mathrm{bulk}}}{2\,\mathrm{A}} \;\mid\; \mathrm{E}_{\mathrm{rel}} = \gamma^{\mathrm{relax}} - \gamma^{\mathrm{fix}} \qquad \text{(Eq. 2)},$$

where $\mathrm{E}^{\mathrm{fix}}_{\mathrm{surface}}$ and $\mathrm{E}^{\mathrm{relax}}_{\mathrm{surface}}$ are the energies of the simulated fixed and relaxed surfaces, N is the number of bulk units contained in the surface model, and A is the area of the created surface.

The surface structural relaxation is calculated as the difference of the distance between the layers for the bulk-truncated system and the relaxed one,

$$\Delta \mathrm{d}_{\mathrm{n}-(\mathrm{n}-1)} = \Delta \mathrm{d}^{\mathrm{relax}}_{\mathrm{n}-(\mathrm{n}-1)} - \Delta \mathrm{d}^{\mathrm{fix}}_{\mathrm{n}-(\mathrm{n}-1)} \qquad \text{(Eq. 3)},$$

where $\Delta \mathrm{d}^{\mathrm{relax}}_{\mathrm{n}-(\mathrm{n}-1)}$ and $\Delta \mathrm{d}^{\mathrm{fix}}_{\mathrm{n}-(\mathrm{n}-1)}$ represent the distance between two consecutive layers in the relaxed and bulk-truncated surface geometries.

5.1.2. Electronic structure

The electronic structure of a solid is considerably different from the molecular orbital energy diagrams obtained for any molecule. Instead of having defined energy levels where orbitals are located, solids have a continuous set of orbitals, named bands, along the energy range. These bands are a result of a combination of the *infinite* number of orbitals that the system has, because of the *infinite* number of atoms, see Figure 5. The integration over the space of the orbitals (bands) yields the Density Of States (*DOS*) as a function of the energy. The DOS is occupied up to the Fermi energy, E_F, the solid equivalent to the Highest Occupied Molecular Orbital (*HOMO*) in molecules.

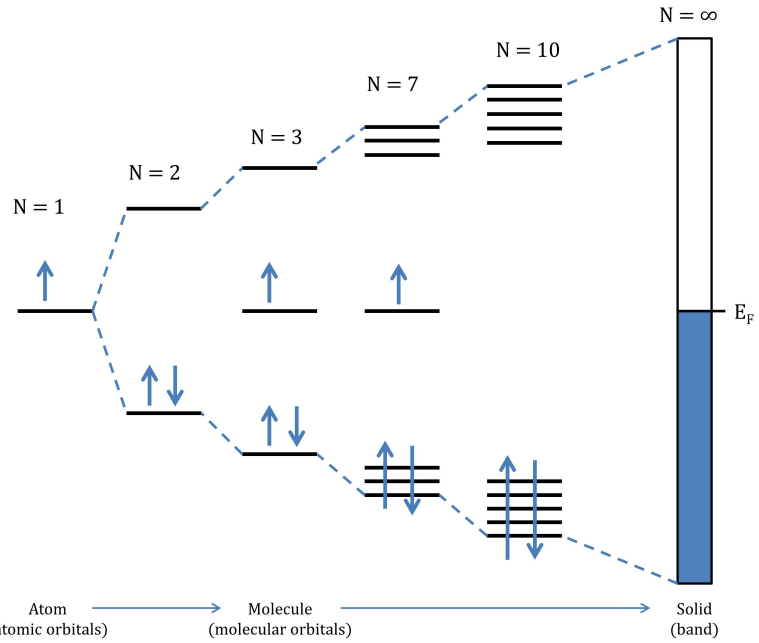

Figure 5. Evolution of the orbitals of a chemical type as a function of the number N of atoms.

Each atom of a solid contributes to the total DOS, and simplifying the global structure to the unit cell, there is also a contribution of each atom of the unit cell to the DOS. Moreover, the contribution of one atom can be itemized into the contributions of the *s*-, *p*-, and *d*-orbitals.

The chemical activity and reactivity of a surface is highly dependent of its electronic structure, but not only. Other factors intimately linked are the stacking pattern and the CN. In order to have a general idea about which materials would feature higher and lower activities without simulating the process of interest itself, these dependences have been studied, as some simple descriptors of general validity of the chemical activity have been proposed.

5.1.3. Chemical descriptors

A descriptor of the chemical activity can be defined as a physicochemical parameter that follows the trend of the chemical activity/reactivity when some of the factors shown before are changed. In previous studies[8-10] some features obtained from the electronic structure were suggested and tested as descriptors: the *d*-band center[8], the width corrected *d*-band center[9], and the maximum of the imaginary part of the *d*-band Hilbert transform.[10]

The *d*-band center, ε_{d}, is a descriptor obtained from the *d*-contribution of a surface atom to the DOS. It is simply defined as the *d*-band gravimetric center, and mathematically calculated with the following equation:

$$\varepsilon_{\mathrm{d}} = \frac{\int_{E_{di}}^{E_{df}} \mathrm{E} \cdot \zeta(\mathrm{E} - \mathrm{E_F})\, dE}{\int_{E_{di}}^{E_{df}} \zeta(\mathrm{E} - \mathrm{E_F})\, dE} \qquad \text{(Eq. 4)},$$

where $\zeta(\mathrm{E} - \mathrm{E_F})$ is the DOS rescaled to the Fermi energy, and the integral limits (E_{di} and E_{df}) are the energies that corresponds to the *d*-band edge (starting point) and tail (ending point). The end of the *d*-band is defined as the energy that would have the last occupied level if it was filled up to a d^{10} electronic configuration.

The *d*-band center has been used in the last two decades to justify and to predict differences of adsorption on transition metals surfaces. A metallic surface with a higher *d*-band center exhibits a higher affinity to adsorb. However, not in all cases this trend is followed, and other descriptors were defined, which included the width of the *d*-band to the expression of the *d*-band center, as a way to include some information about the shape of the DOS in the descriptor. This new descriptor is the width corrected *d*-band center:

$$\varepsilon_{\mathrm{d}}^{\mathrm{W}} = \varepsilon_{\mathrm{d}} + \frac{\Delta \mathrm{E}}{2} \qquad \text{(Eq. 5)},$$

where $\Delta \mathrm{E} = E_{df} - E_{di}$. There is also another descriptor recently defined as a better one than the previous, the maximum point of the Hilbert transform of the *d*-band, ε_{u}. It is calculated applying the Hilbert transform to the DOS, and taking the energy of the highest peak.[10]

At this point, all the descriptors under study are defined. Let us then study how to computationally obtain all the needed information, DOS, in order to calculate the explained parameters for bulks and surfaces.

5.2. COMPUTATIONAL TREATMENT

The progresses over the last years in computer power, supercomputing, and highly parallel computing, as well as on the implementation of new computational methods, have provided us a high capacity to carry out studies of solid structures based on quantum chemistry. As it has been previously shown, solids can be classified depending on their structure as crystalline or amorphous, and the computational treatment for each type is different. On the following, only

the treatment of crystalline studies is explained, which is the case of the metals studied in this work.

The computational study of a crystalline solid could be tackled from two different points of view. The first one is the finite (cluster) model, which consists in simulating a number of atoms large enough in order to correctly represent the system, but ignoring the fact that the material is much vaster than the portion under study. The principal advantage of this way is the possibility to apply all the most stablished wavefunction methods of the quantum chemistry to the system, but always dealing with the limitations of the computational costs of simulating a high number of atoms.

The second point of view is the so-called periodic model, and is based on exploiting in a computational way the repetitiveness previously shown for crystalline structures, so as to simplify the calculations, applying only the quantum chemistry calculation to the defined unit cell. To make this approximation is not an impediment for obtaining local properties, but also is suited to gain macroscopic properties estimations. Next, one of the most used methods in electronic structure studies for solids is explained, DFT. Last, the Bloch theorem is presented, which deals with the application of the periodic model in computational calculations.

5.2.1. Density functional theory

DFT[11] is one of the most common procedures for obtaining results of the electronic structure of systems with a high number of atoms, as is a good balance in between accuracy and computational cost, also suited for carrying out calculations using a large basis set. The electronic structure calculation of crystalline solids is included among its many fields of applicability.

The capability of DFT to study large systems is grounded in the sense that this method establishes that the energy of a ground state can be calculated from the monoelectronic density function, ρ, and, as a result, only depends on three variables, which are the three space coordinates that stablish the position where the density is evaluated. This point represents a big advantage in front of other methods that try to solve the Schrödinger equation (wavefunction methods), because wavefunctions are functions which depend on 4N variables, where N is the number of electrons. This is a main argument why the computational cost of the same calculation is lower in DFT (sketch 1).

DFT	Wavefunction methods
$\rho = \mathrm{f}(3 \text{ variables})$	$\Psi = \mathrm{f}(4\mathrm{N} \text{ variables})$
$\mathrm{E}_0 = \min_{\rho} \mathrm{E}[\rho]$	$\hat{\mathrm{H}}\,\Psi_0 = \mathrm{E}_0\,\Psi_0$

Sketch 1: DFT *versus* wavefunction methods.

However, the disadvantage of DFT is that the exact relation between the energy and the electronic density is not known, and it has to be adjusted to each system according to its characteristics. Because of the parametrization, the *exact* energy of a determinate state can never be obtained from a DFT calculation although highly accurate estimates are reachable. Next, foundations of the DFT method are explained.

5.2.1.1. Main concepts

The main idea of DFT is to work with the electronic density function instead of the wavefunction. The relation between the electronic density and the energy is expressed as a functional, $\mathrm{E}[\rho]$. The exact dependence on ρ is unknown, and some terms have to be approximated (the exchange and correlation functional) in order reach the applicability.

Under any of these approximations, when ρ is known, its respective energy can be easily calculated. Because of this, only a method to get ρ for the system of interest is needed. This method consists in an iterative process, which, from a starting electronic density (ρ_i), generates the one for the ground state (ρ_0). The iterative process is needed because the factors that affect the ρ_i in the process to obtain ρ_0 (some terms of the Hamiltonian of the system) are also a function of ρ.

Summarizing, the procedure of DFT is: first, to choose an approximation for the unknown terms of $\mathrm{E}[\rho]$ (shown in the 5.2.1.4. section); then, obtain the electronic density function for the ground state with an iterative procedure (developed in the 5.2.1.3. section); and finally, use the $\mathrm{E}[\rho]$ expression to get the energy for the ground state. These aspects are treated in better detail in the following sections.

5.2.1.2. Development of the method

The foundations of the wavefunction methods are based in the resolution of the Schrödinger equation:

$$\hat{H}\,\Psi = E\,\Psi \qquad \text{(Eq. 6)}.$$

More specifically, after applying the Born-Oppenheimer approximation, which reduces the number of variables by fixing the nuclear ones, the problem is reduced to solving the *electronic* Schrödinger equation:

$$\hat{H} = \hat{T}_{el} + \hat{T}_{nuc} + \hat{V}_{el} + \hat{V}_{nuc} + \hat{V}_{nuc-el} \qquad \text{(Eq. 7)},$$

$$\hat{H}_{el} = \hat{T}_{el} + \hat{V}_{el} + \hat{V}_{nuc-el} \quad | \quad \hat{H}_{el}\Psi = E_{el}\,\Psi \qquad \text{(Eq. 8)},$$

where $\hat{H}$ is the Hamiltonian, which is composed of the kinetic energy components of the nuclei ($\hat{T}_{nuc}$) and of the electrons ($\hat{T}_{el}$), the potential repulsion between nuclei ($\hat{V}_{nuc}$) and between electrons ($\hat{V}_{el}$), and the potential attraction between nuclei and electrons ($\hat{V}_{nuc-e}$). $\hat{H}_{el}$ is the electronic Hamiltonian, and contains only the electronic components of the Hamiltonian of the system.

To know an operator also allows knowing its possible eigenvalues and eigenfunctions. In this sense one can think that by knowing the Hamiltonian of a system, its wavefunctions and energetic levels are defined. This is true only for the simplest cases, like the monodimensional potential box. In more complex systems, which have more chemical interest, it is not possible to analytically solve the Schrödinger equation, and it is necessary to use different existent wavefunction methods, like Hartree-Fock (HF), coupled-cluster (CC), configurations interaction (CI), etc.

The DFT method, by contrast, faces the problem in a different way. The Hohenberg-Kohn theorems established the background theory for the method that implies that, instead of searching a wavefunction, one tries to find an electronic density function equal to the exact one of the system, which describes how it is related with the energy of the system ground state.

The electronic density function $[\rho(\vec{r})]$ is the squared modulus of the wavefunction (Ψ), so working with it instead of the wavefunction provides a worse description of the system, because, as can be seen in Eq. 10, the information of the complex part of the function ($e^{i\cdot f(\vec{r})}$) is lost when the electronic density is obtained. There are infinite wavefunctions with the same electronic density. In Eq. 9, $\vec{r}_n$ and w_n are the space and spin coordinates for each electron.

$$\rho(\vec{r}) = \int \Psi^*(\vec{r}_1, w_1 \dots \vec{r}_N, w_N)\Psi(\vec{r}_1, w_1 \dots \vec{r}_N, w_N)\, d_{w_1} d_{\vec{r}_2} d_{w_2} \dots d_{\vec{r}_N} d_{w_N} \qquad \text{(Eq. 9)},$$

$$\rho \quad \leftrightarrow \quad |\Psi| \leftarrow \quad \Psi = |\Psi| \cdot e^{i \cdot f(\vec{r})} \qquad \text{(Eq. 10)}.$$

The relation between the electronic density function and the energy starts on the variational theorem, which exposes that the energy of a ground state is the minimum value of the variational integral for all the wavefunctions of the Hilbert space:

$$E_0 \leq \langle \Psi | \hat{H} \Psi \rangle \qquad \text{(Eq. 11)}.$$

Starting from this premise, and considering the ρ definition (Eq. 9), the energy-electronic density relation is posed as a double minimization. The first one consists in finding the wavefunction which has the lowest variational integral $\langle \Psi | \hat{H} \Psi \rangle$ for each possible ρ of the system, and the second one is just to search the lowest electronic density energy among all the electronic densities. This explanation is formally described as follows; being defined the energy functional $E[\rho]$ as:

$$E_0 = \min_{\rho} \left(\min_{\Psi \to \rho} \langle \Psi | \hat{H} \Psi \rangle \right) = \min_{\rho} \left(\langle \Psi_\rho^{min} | \hat{H} \Psi_\rho^{min} \rangle \right)$$

$$E[\rho] = \min_{\Psi \to \rho} \langle \Psi | \hat{H} \Psi \rangle \quad | \quad E_0 = \min_{\rho} E[\rho] \qquad \text{(Eq. 12)}.$$

In the previous expression, the Hamiltonian can be broken down as described in Eq. 8:

$$\langle \Psi_\rho^{min} | \hat{H} \Psi_\rho^{min} \rangle = \langle \Psi_\rho^{min} | (\hat{T}_{nuc} + \hat{V}_{el}) \Psi_\rho^{min} \rangle + \langle \Psi_\rho^{min} | \hat{V}_{nuc-el} \Psi_\rho^{min} \rangle \qquad \text{(Eq. 13)},$$

where $\langle \Psi_\rho^{min} | \hat{V}_{nuc-el} \Psi_\rho^{min} \rangle$ is a property of the system that can be related with the electronic density as follows:

$$\langle \Psi_\rho^{min} | \hat{V}_{nuc-el} \Psi_\rho^{min} \rangle = \int_{\vec{r}} v_{ne}(\vec{r})\ \rho(\vec{r})\, d\vec{r} \qquad \text{(Eq. 14)},$$

where $v_{ne}(\vec{r})$ is the potential that an electron is subjected to at a $\vec{r}$ position due to all the nuclei. This term is named external potential, and is a known term if the nuclei positions are defined. Last, the notation $F[\rho]$ is used to the first summatory in Eq. 13 to yield:

$$E[\rho] = F[\rho] + \int_{\vec{r}} v_{ne}(\vec{r})\ \rho(\vec{r})\, d\vec{r} \qquad \text{(Eq. 15)},$$

$$F[\rho] = \left\langle \Psi_\rho^{min} \middle| \left(\hat{T}_{el} + \hat{V}_{el}\right) \Psi_\rho^{min} \right\rangle = \left\langle \Psi_\rho^{min} \middle| \hat{T}_{el}\, \Psi_\rho^{min} \right\rangle + \left\langle \Psi_\rho^{min} \middle| \hat{V}_{el}\, \Psi_\rho^{min} \right\rangle$$
$$F[\rho] = T[\rho] + V_{el}[\rho] \qquad \text{(Eq. 16).}$$

The $F[\rho]$ functional is universal, in the sense that it only depends on the number of electrons of the system, and not of its complexity. Given that, if its expression is known for a N-electron simple case, it could well be applied to any other N-electron system. However, the expressions for $T[\rho]$ and $V_{el}[\rho]$ are unknown.

Hohenberg and Kohn also demonstrated that the external potential (v_{ne}) is a function of the electronic density in the following way:

$$v_{ne} = -\left(\frac{\partial F[\rho]}{\partial \rho_0}\right) \qquad \text{(Eq. 17),}$$

which is an important fact, as indicates that the electronic density defines the positions and the charges of the nuclei.

The theoretical description for the DFT method ends at this point. When the term $F[\rho]$ was known, the energy could be obtained minimizing Eq. 15; but, because it is not, all the DFT methods try to parametrize this functional. The most stablished method is the DFT-KS, developed by Kohn and Sham.

5.2.1.3. DFT-KS

The main idea of Kohn and Sham (*KS*) was to solve the unknown functional $F[\rho]$ by relating the system of interest (real system) with another N-electron system with the same ρ, in where the electrons do not interact among themselves (KS system). To do this, it is necessary to develop $F[\rho]$ with information of the KS system, gaining as a result an expression for $E[\rho]$ that allows obtaining results. The method also suggest an iterative process to obtain ρ.

It is necessary to define $F[\rho]$ because the $T[\rho]$ and the $V_{el}[\rho]$ terms are unknown. In order to solve it, it is necessary to apply the theory described previously to the KS system. A $F^{KS}[\rho]$ is obtained, which does not have the $V_{el}[\rho]$ term because the KS system is defined without interactions between electrons. Therefore, because of this non-interaction, the kinetic energy term is also easily calculated:

$$F^{KS}[\rho] = T^{KS}[\rho] \quad | \quad T^{KS}[\rho] = \langle \Psi_\rho^{KS} | \hat{T}_{el} \Psi_\rho^{KS} \rangle = \sum_{i=1}^{N} c_i \left\langle \phi_i^{KS} \left| -\frac{\nabla^2}{2} \phi_i^{KS} \right\rangle \right. \quad \text{(Eq. 18).}$$

Furthermore, the electronic repulsion term (V_{el}) can be described without considering quantum aspects with the Coulomb law, obtaining the following equation:

$$J[\rho] = \int_{\vec{r}_1} \int_{\vec{r}_2} \frac{\rho(\vec{r}_1)\rho(\vec{r}_2)}{r_{12}} \, d\vec{r}_1 \, d\vec{r}_2 \quad \text{(Eq. 19).}$$

In order to supply the unknown terms of $F[\rho]$, the following operation is done:

$$F[\rho] = T[\rho] + V_{el}[\rho] = T[\rho] + V_{el}[\rho] + T^{KS}[\rho] - T^{KS}[\rho] + J[\rho] - J[\rho] \quad \text{(Eq. 20).}$$

A different order of the terms allows the definition of the exchange and correlation potential $E_{xc}[\rho]$:

$$F[\rho] = T^{KS}[\rho] + J[\rho] + (T[\rho] - T^{KS}[\rho] + V_{el}[\rho] - J[\rho]) \quad \text{(Eq. 21),}$$

$$E_{xc}[\rho] = T[\rho] - T^{KS}[\rho] + V_{el}[\rho] - J[\rho] \quad \text{(Eq. 22).}$$

The exchange and correlation potential represents the error of assuming that the kinetic energy of the real system is the same as the one of a KS system, plus that the electronic interactions have classical behavior. The dependence of the functional with the electronic density is not known, but several parametrizations exist, further described. The value for the $E_{xc}[\rho]$ must be small in comparison with $F[\rho]$, because the differences between the kinetic energy of the two systems and the quantum corrections in the electronic repulsions will be also small.

$F[\rho]$ is finally defined as:

$$F[\rho] = T^{KS}[\rho] + J[\rho] + E_{xc}[\rho] \quad \text{(Eq. 23).}$$

At this point, the dependence of all the functionals with the electronic density is known or parametrized, so it is easy to obtain a value as a result of this expression.

If the new $F[\rho]$ definition is substituted in Eq. 15:

$$E[\rho] = T^{KS}[\rho] + J[\rho] + E_{xc}[\rho] + \int_{\vec{r}} v_{ne}(\vec{r}) \, \rho(\vec{r}) \, d\vec{r} \quad \text{(Eq. 24),}$$

it ends with all the terms substituted for their own expressions; the energy can be calculated, after parametrizing $E_{xc}[\rho]$, from the following equation:

$$E[\rho] = \langle \Psi_\rho^{KS} | \hat{T}_{el} \Psi_\rho^{KS} \rangle + \int_{\vec{r}_1} \int_{\vec{r}_2} \frac{\rho(\vec{r}_1)\rho(\vec{r}_2)}{r_{12}} \, d\vec{r}_1 \, d\vec{r}_2 + E_{xc}[\rho] + \int_{\vec{r}} v_{ne}(\vec{r}) \, \rho(\vec{r}) \, d\vec{r} \quad \text{(Eq. 25)},$$

where only ρ for the ground state is needed to obtain its respective energy.

In order to get ρ, Kohn and Sham suggested an iterative method that leverages the description of the KS system, which has a different Hamiltonian ($\hat{H}^{KS}$). Because of the non-interaction, the Hamiltonian can be separated in monoelectronic terms, and the monoelectronic Kohn-Sham operator ($\hat{h}^{KS}$) can be defined as:

$$\hat{H}^{KS} = \hat{T}_{el} + \hat{V}^{KS} = \sum_{i=1}^{N} \left(-\frac{\nabla^2}{2} + v^{KS} \right) = \sum_{i=1}^{N} \hat{h}^{KS} \quad \text{(Eq. 26)},$$

where $\hat{V}^{KS}$ is the external potential operator, and describes the potential that an electron would feel in the KS system. It includes the nucleus-electron potential and some information about the interelectronic repulsion as a ρ-depending parametrization. To have a separable Hamiltonian ensures that the exact wavefunction of the system can be expressed as just one Slater determinant of N spinorbitals, where N is also the number of electrons:

$$\Psi_0^{KS} = \frac{1}{\sqrt{N!}} \left| \phi_i^{KS} \dots \phi_N^{KS} \right| \quad \text{(Eq. 27)},$$

$$\hat{h}^{KS} \phi_i^{KS} = \varepsilon_i^{KS} \phi_i^{KS} \quad \text{(Eq. 28)}.$$

Obtaining these spinorbitals is not a direct step. The eigenvalues equation (Eq. 28) has to be solved with an iterative process, because v^{KS} is a function of ρ.

To know the v^{KS} expression it is necessary to remember Eq. 17. Knowing that in the KS system $F^{KS}[\rho] = T^{KS}[\rho]$, v^{KS} will be:

$$v^{ks} = -\left(\frac{\partial T^{KS}[\rho]}{\partial \rho_0} \right) \quad \text{(Eq. 29)}.$$

When Eq. 29 is derived,

$$\left(\frac{\partial F[\rho]}{\partial \rho_0} \right) = \left(\frac{\partial T^{KS}[\rho]}{\partial \rho_0} \right) + \left(\frac{\partial J[\rho]}{\partial \rho_0} \right) + \left(\frac{\partial E_{xc}[\rho]}{\partial \rho_0} \right) \quad \text{(Eq. 30)},$$

$v_{xc}(\vec{r}_1)$ is defined,

$$v_{xc}(\vec{r}_1) = \left(\frac{\partial E_{xc}[\rho]}{\partial \rho_0}\right) \quad \text{(Eq. 31)},$$

and the functional of Coulombic repulsions is derived,

$$\left(\frac{\partial J[\rho]}{\partial \rho_0}\right) = \int_{\vec{r}_2} \frac{\rho_0(\vec{r}_2)}{r_{12}}\, d\vec{r}_2 \quad \text{(Eq. 32)},$$

a final expression for the monoelectronic external potential for the KS system is then achieved:

$$v^{KS}(\vec{r}_1) = v_{ne}(\vec{r}_1) + \int_{\vec{r}_2} \frac{\rho_0(\vec{r}_2)}{r_{12}}\, d\vec{r}_2 + v_{xc}(\vec{r}_1) \quad \text{(Eq. 33)}.$$

Knowing the expression for the external potential of the KS system, the iterative process that allows obtaining ρ_0 can be defined. First, an initial ρ is needed, which defines the Hamiltonian. With this Hamiltonian, the eigenvalues equation can be solved, and a new ρ can be calculated:

$$\rho(\vec{r}) = \sum_{i=1}^{N} \left|\phi_{i(\vec{r})}\right|^2 \quad \text{(Eq. 34)}.$$

This cycle is repeated until autoconvergence, and when the converged electronic density is obtained, the energy of that electronic density can be calculated as it is previously described. In Figure 6 a scheme of the DFT process is shown, and each step of the cycle is related with the needed equations developed previously.

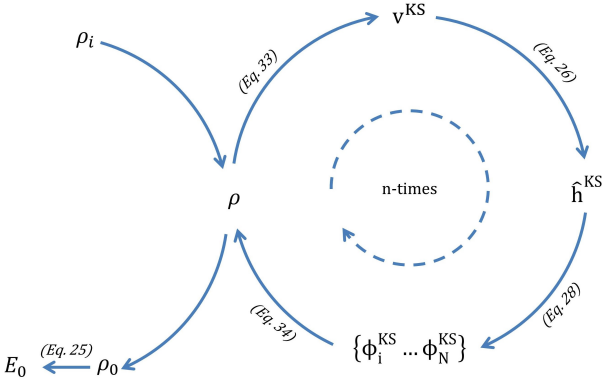

Figure 6. Scheme of the DFT iterative process.

5.2.1.4. Exchange and correlation functional approximations

The only missing information for the application of DFT is, at this point, the approximated expressions for the exchange and correlation (*xc*) functional. These expressions have been studied for many years trying to find the exact form of the functional, because knowing its form would be the key for obtaining exact calculations. The studies on xc functionals are a very large branch of DFT, and only the general idea of each one is here explained.

Approximate expressions for the exchange and correlation functional are usually sorted according to how near they are from the exact form. Figure 7 illustrates this idea. More accurate functionals are developed from previous approximations, and include some improvements. Let us see the different existent approximations.

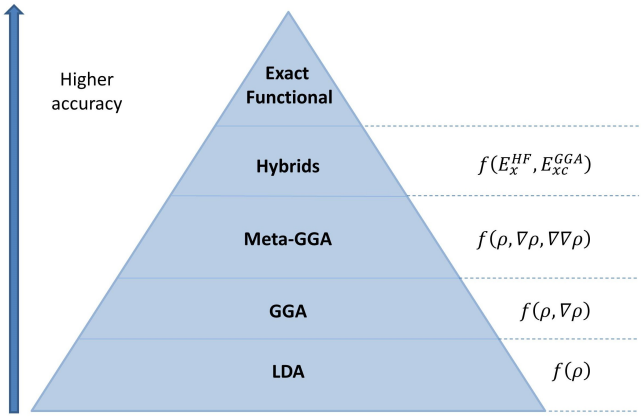

Figure 7. Scheme of the different existent xc functionals for DFT calculations, and how near they are from the exact functional. Note that this scheme is proposed to be true for molecular simulations.

The local density approximation (*LDA*) is based on the supposition that the electronic density does not change much with the position, and, as a result, its derivative is approximated to zero. Under this condition, the xc functional can be separated in two terms:

$$\mathrm{E_{xc}^{LDA}}[\rho] = \mathrm{E_c}[\rho] + \mathrm{E_x}[\rho] \qquad \text{(Eq. 35)},$$

where the value of $\mathrm{E_c}[\rho]$ is parametrized with standard values provided from calculations made when this approximation was stablished. $\mathrm{E_x}[\rho]$ takes the following dependence with ρ:

$$E_x[\rho] = -\frac{3}{4}\left(\frac{3}{\pi}\right)^{\frac{1}{3}} \rho(\vec{r})^{\frac{1}{3}} \quad \text{(Eq. 36).}$$

With this first approximation to the xc functional, there are no missing parameters to be known, and calculations can be carried out. LDA works well for some systems and properties, like interatomic distances and properties of metals, because, as a result of their periodicity and electronic delocalization, they are near to the approximation of $\nabla\rho(\vec{r}) = 0$. However, this approximation does not work well for other chemical systems, and other functionals should be used.

Another widely used approximation is the general gradient approximation (GGA). This is a more accurate than LDA, because it considers in addition to the electronic density, its derivative.

$$E_{xc}^{GGA}[\rho] = \int f(\rho, \nabla\rho)\, d\vec{r} \quad \text{(Eq. 37).}$$

Different flavors for this approximation have been established for many years, and the one used in this study is PBE.[6] An improved approximation to that is when $E_{xc}[\rho]$ is also a function of the ρ second derivate, the so called meta-GGA, where TPSS[7] is an example. This xc is also used in this study.

As appears at Figure 7, there are better existing methods to approximate $E_{xc}[\rho]$ that are nearly the exact form of the functional for a molecular system; the hybrids functionals. These functionals are based on a combination of the exchange energy obtained by HF with some GGA contributions. One popular is known as the 3-parameter, Becke-Lee-Yang-Parr (B3LYP).[12] However, in some cases, these improvements do not justify the extra computational costs. Moreover, in crystalline solids systems, especially metals, the gradation shown in Figure 5 is not always followed, and GGA or meta-GGA performs better.[13] This is the main reason why PBE and TPSS were chosen.

Note that with the theory described DFT can only be applied to molecules or solids under the finite model condition. The largest advantages in computational costs appeared when studies of solids started to be carried out with periodic boundary conditions. These periodic conditions were computationally treated by the physicist Felix Bloch, and announced by the Bloch theorem.[14]

5.2.2. Bloch theorem

The Bloch theorem tries to take advantage of the repetitiveness of the structure of a crystalline solid in order to reduce the computational costs of the calculations. The main idea is to have a wavefunction whose properties are the same if a translation in any direction of the cell by an entire amount is applied. This is achieved when the wavefunction value is the same if the position in where it is evaluated changes in a multiple of one of the cell parameters:

$$\Psi(\vec{r}) = \Psi\left(\vec{r} + \vec{R}\right) \qquad \text{where } \vec{R} \in n \cdot (\vec{a}, \vec{b}, \text{or } \vec{c}) \qquad \text{(Eq. 38).}$$

The Bloch theorem also established the wavefunctions that accomplish this condition, which are the product of two functions, the first one is a plane wave, and the second one contains the periodicity term.

$$\Psi(\vec{r}) = e^{ik\vec{r}} v_{i(\vec{r})} \qquad \text{(Eq. 39).}$$

This wavefunction allows describing the macroscopic system only using one unit cell, and greatly reduces the computational costs. The peculiarity of this wavefunction is that the system must be described in a different lattice than the real lattice, this is, the reciprocal lattice. The space vectors of the reciprocal lattice are the inverse to the real lattice one; so, as a rule-of-a-thumb, the larger vector in the real lattice is, the shorter is in the reciprocal lattice. The Bloch theorem is a very useful tool to apply in computational studies of periodic solids.

6. COMPUTATIONAL DETAILS

All calculations in this work were carried out using the Vienna *Ab Initio* Simulation Package (VASP)[15] and Projected Augmented Wave (PAW)[16] pseudopotentials. PBE and TPSS functionals are used. The cutoff energy for the plane-wave basis set is 415 eV. A tetrahedral method smearing algorithm with a width of 0.2 eV was used, yet final energies were extrapolated to 0 K (no smearing). The Monkhorst-Pack **k**-points grid used for bulk calculations is a 7×7×7 grid, and 7×7×1 for surfaces. The three surfaces under study are simulated always with a unit cell containing 12 atoms, which supposes a six-layer arrangement for (0001) and $(10\bar{1}0)$ surfaces, and twelve-layer arrangement for $(11\bar{2}0)$ surface, always with a vacuum of 10 Å. This vacuum is enough to avoid interactions between translationally repeated slabs. The surfaces were calculated twice, first with all the atom positions frozen, and then letting all the atoms relax, in order to get fixed and relaxed surface energies.

The density of states for each surface was reached with a single-point calculation on the relaxed geometry, previously obtained. This calculation was carried out with a number of bands of 240 (20×number of atoms), and with a sampling of the energy range of almost 10000 points.

The calculation of the descriptors was carried out using an own programmed code using python language, which allows to automatically obtain the values for the descriptors of interest applying the theory previously exposed in section 5.1.3, needing only the input from the density of states.

7. RESULTS AND DISCUSSION

7.1. BULK

Bulk calculations are made for all *hcp* transition metals in order to obtain the optimized structures for the simulation of the surfaces. Moreover, they are as well a good checkpoint because the obtained values can be compared with previous calculations and some experimental results. For the PBE and TPSS functionals, cohesive energies, E_{coh}, and shortest internuclear distances, δ, are obtained, as shown in Table 1.

Metal	PBE_{calc}		PBE_{prev}[17]		$TPSS_{calc}$		$TPSS_{prev}$[18]		Exp.[17]	
	E_{coh}	δ	E_{coh}	δ	E_{coh}	δ	E_{coh}	δ	E_{coh}	δ
Sc	4.18	3.21	4.12	3.21	4.11	3.18	4.21	3.20	3.9	3.25
Y	4.12	3.52	4.13	3.54	4.26	3.53	4.23	3.52	4.39	3.56
Ti	5.42	2.85	5.46	2.88	5.19	2.82	5.47	2.86	4.84	2.90
Zr	6.23	3.15	6.16	3.20	6.43	3.14	6.30	3.18	6.29	3.18
Hf	6.37	3.11	6.4	3.14	6.63	2.98	6.53	3.11	6.42	3.13
Tc	6.80	2.69	6.85	2.72	6.45	2.69	7.18	2.70	7.13	2.71
Re	7.76	2.71	7.82	2.76	7.86	2.72	8.25	2.74	8.02	2.57
Ru	6.56	2.65	6.67	2.66	6.16	2.64	7.10	2.64	6.74	2.66
Os	8.17	2.68	8.29	2.69	7.07	2.67	8.46	2.69	8.17	2.68
Co	5.30	2.44	5.27	2.40	5.76	2.52	6.21	2.44	4.43	2.50
Zn	1.10	2.71	1.12	2.89	1.64	2.61	1.34	2.52	1.35	2.91
Cd	0.75	3.11	0.73	3.15	0.83	2.99	0.96	2.92	1.16	3.29

Table 1. Bulk cohesive energies (in eV/atom) and shortest internuclear distance (in Å) calculated (calc) or previously obtained (prev) using a comparable set up, as well as experimental (Exp.) values.

With the purpose of easily compare the xc functionals, and also to have a general idea about the accuracy of the obtained calculations, the mean percentage error (MPE) and the mean absolute percentage error (MAPE) are calculated. The MPE is defined as the percentage deviation of a value (x_i) from its reference value (x_i^{Ref}), and the MAPE is the same calculation but considering the absolute value of the deviation, as MPE can lead to cancellation of errors:

$$MPE = \frac{(x_i - x_i^{Ref})}{x_i} \cdot 100 \quad \text{(Eq. 40)},$$

$$MAPE = \frac{|x_i - x_i^{Ref}|}{x_i} \cdot 100 \quad \text{(Eq. 41)}.$$

The MPE gives an idea about how near are the values obtained from the reference ones, but it is especially suited to observe signed systematic errors. The MAPE takes it in account and expresses the averaged difference without considering whether there is an excess or a defect of error. MAPE also expresses as well whether there is a cancellation of errors in MPE. The obtained averages for MPE and MAPE for the cohesive energies and for the shortest internuclear distances are shown in Table 2.

	E_{coh}				δ			
	PBE		**TPSS**		**PBE**		**TPSS**	
	Prev.	**Exp.**	**Prev.**	**Exp.**	**Prev.**	**Exp.**	**Prev.**	**Exp.**
MPE	-0.2	-5.2	-5.0	-1.9	-1.2	-1.4	0.0	-2.4
MAPE	1.1	10.9	8.7	11.6	1.5	2.3	1.5	3.5

Table 2. Obtained mean MPE and MAPE for cohesive energies, E_{coh}, and shortest internuclear distances, δ, compared to previous calculations,[17,18] and experimental values.[17]

The obtained results for the cohesive energies are in excellent concordance with previous calculations at PBE level, as the MAPE is 1.1%. The concordance of TPSS is good (8.7%). None of them deliver systematic over- or underestimations. As far as shortest internuclear distances are concerned, the values obtained with both xc functionals excellently agree with previous estimations (MAPE values of 1.5% in both cases). Notice that PBE estimates seem more robust and reliable, as vary less according to computational set ups compared to TPSS values.

Concerning the experimental data, there is also high agreement for both functionals, despite the higher MAPE in cohesive energies. So, it can be truly affirmed that the systems are well described with PBE but also with TPSS. The comparison for each xc functional shows that there is no big difference among them (10.9% for PBE and 11.6% for TPSS, in the case of E_{coh} and 2.3% for PBE and 3.5% for TPSS for δ); so, even though PBE seems slightly better than TPSS,

with the obtained results one cannot clearly state one of these functionals as best suited for the description of the bulk systems under study.

Looking for possible trends for the cohesive energy values, Figure 8 is plotted. It is there observable an increasing trend when going down a group of the periodic table, except for the d^{10} metals, which goes in concordance with what could be expected. The overall trend could be linked to less local *d* shells for 4*d* and 5*d* elements, a fact that would favor (strengthen) the metal bonding.

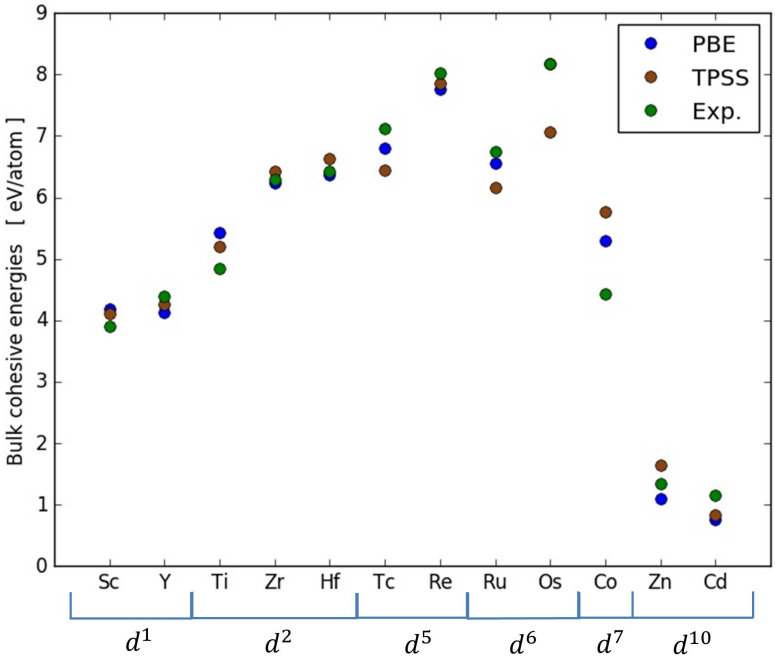

Figure 8. Cohesive energies obtained for the *hcp* transition metal bulks.

There is also an increase of the bulk cohesive energy along the period up to d^5 metals. When the *d*-band is being occupied, until the d^5 orbitals are full, the added electrons go to bonding orbitals, which make the bond stronger, and as a result implies an increase of the cohesive energy. However, when d^5 orbitals are full, further electrons go to antibonding orbitals, which cause a decrease of the bond strength, and also of the cohesive energy. This kind of pattern is known as volcano shape, and is usual in the study of solid properties for transition metals due to the electronic changes while going along a series.

7.2. SURFACES

As exposed in the objectives, different surface properties are studied. The first one is the relaxed surface energy (γ^{relax}), and it was obtained for the three surfaces under study using PBE and TPSS. These surfaces were simulated with unit cells that contains 12 atoms in each case, which are arranged in 6 layers for (0001) and $(11\bar{2}0)$, and 12 layers for $(10\bar{1}0)$; and with 10 Å of vacuum. The values obtained are shown in Table 3.

γ^{relax} [J/m²]								
Metal	**PBE**			**TPSS**			**Prev.[19]**	**Exp.[19]**
	(0001)	$(10\bar{1}0)$	$(11\bar{2}0)$	(0001)	$(10\bar{1}0)$	$(11\bar{2}0)$	(0001)	(0001)
Sc	1.22	1.45	1.22	1.48	1.74	1.28	1.83	1.28
Y	0.94	1.17	0.99	1.04	0.97	1.00	1.51	1.13
Ti	2.02	2.10	1.87	2.46	2.28	2.17	2.63	1.99
Zr	1.62	1.78	1.64	1.90	1.80	1.97	2.26	1.91
Hf	1.69	2.01	1.80	2.06	2.50	2.12	2.47	2.19
Tc	2.01	3.27	2.69	2.40	3.77	3.35	3.69	3.15
Re	2.35	3.94	3.10	2.86	2.64	3.39	4.21	3.63
Ru	2.04	3.27	3.05	2.62	5.16	3.71	3.93	3.04
Os	2.21	4.05	3.63	2.37	4.48	3.96	4.57	3.44
Zn	0.36	1.04	0.80	1.55	2.37	1.64	0.99	0.99
Cd	0.30	0.64	0.49	0.59	1.24	0.62	0.59	0.76

Table 3. Obtained values for γ^{relax} for (0001), $(11\bar{2}0)$, and $(10\bar{1}0)$ surfaces at PBE and TPSS level; previous calculations (Prev.) and experimental data (Exp.).

Due to the few studies which describe the surface energies for *hcp* transition metals, the obtained values can difficultly be compared. Note that the previous calculations were not done with one of the functionals that have been used in this work, and the experimental surface energy is found described only pointing to the (0001) surface.

The results for Cobalt were not reached at the time of writing this work since there were difficulties in converging the correct minimum of its potential energy surface. Cobalt is the only element of the ones studied which is magnetic, and using the same unit cells that have been

used for the others provides a wrong description of the system. The problem appears to be due to magnetic coupling, which has a large range scope, and produces an interaction between the unit cells simulated. It has been proven that the results obtained for Cobalt significantly change when a larger vacuum is used, and also when the number of layers is increased. The calculations that test it were done for the (0001) surface for two different unit cells; one containing 6 layers and a vacuum of 20 Å, and another containing 12 layers and a vacuum of 20 Å. Further calculations should be done in order to test the optimum vacuum and number of layers that do not show significant magnetic coupling, and so that, allow for obtaining converged surface properties. Because of this, Cobalt is excluded from the following analysis.

Focusing first on the (0001) surface, the comparison between the obtained values and previous calculations, as well as with experimental data is done by obtaining MPE and MAPE for the both functionals. The results are shown in Table 4.

γ^{relax} (0001) [J/m^2]				
	PBE		**TPSS**	
	Prev.	**Exp.**	**Prev.**	**Exp.**
MPE	-59%	-56%	-29%	-9%
MAPE	60%	57%	36%	23%

Table 4. Obtained mean MPE and MAPE for relaxed surface energies, compared to previous calculations and experimental values.[19]

With the obtained results it can be seen that TPSS provides a better description of the system, as is in a better agreement with the experimental data as well as with the previous calculations. PBE shows a systematic error giving lower values in practically all cases.

Looking for a possible explanation for these high differences with respect the experimental data and the calculations done, previous studies stated that experimental surface energy is not ascribed to a particular surface ending, but to a mixure of surfaces. Wulff construction shapes to minimize overall surfaces tension point towards a mixture of 33% of (0001) and a 67% of $(10\bar{1}0)$.[20] So, probably, the surface energy given as an experimental data for the (0001) surface, is not really that particular surface, but the previously named combination. With that, surface energies are recalculated using the previously contribution percentages of each surface

energy, and the MPE and MAPE obtained in the comparison with the same experimental data are shown in Table 5.

γ^{relax} [J/m²]		
	PBE	**TPSS**
MPE	-9.6%	10.4%
MAPE	11.7%	19.7%

Table 5. Obtained mean MPE and MAPE for relaxed surface energies using 66.7%of the $(10\bar{1}0)$ surface energy, and 33.3% of the (0001); compared to experimental data.[19]

Clearly, this weighting greatly improves the accuracy of the results, and the obtained MPE and MAPE show that PBE describes quite better the surface energies than TPSS does (11.7% of averaged deviation for PBE in front of 19.7% of averaged deviation for TPSS). This in turn goes along with a slightly better accuracy of PBE compared to TPSS in describing their bulks.[17]

In order to easily compare between metals and surfaces, the PBE surface energies are plotted in Figure 9.

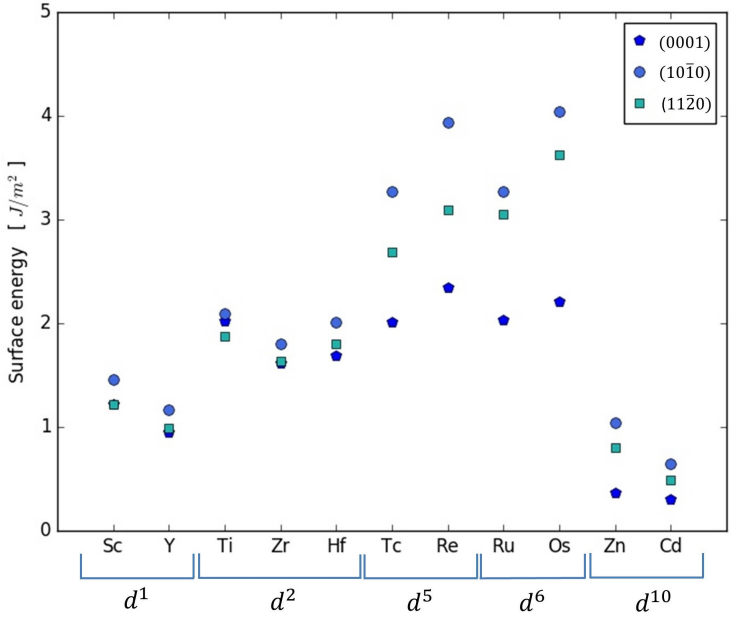

Figure 9. PBE surface energies for the three surfaces under study.

The first evidence that can be extracted from Figure 9 is the most stable surface. Regard that surface energy represents the energy needed for creating the surface from the initial bulk structure. The trend in Figure 9 is that the (0001) surface is the most stable, followed by the $(11\bar{2}0)$, and letting as least stable the $(10\bar{1}0)$ surface. This is not in concordance with the previously commented rule that those surfaces with the highest CN are the most stable, as the CN for these surfaces are 9 for the (0001), 8 for the $(10\bar{1}0)$ and 7 for the $(11\bar{2}0)$. Quantitatively, the (0001) surface energy is a 32% lower than the $(11\bar{2}0)$, and a 57% lower than the $(10\bar{1}0)$.

Also, for studying the differences between both functionals under inspection, the difference in percentage for the obtained relaxed surface energies at PBE and TPSS level are calculated as

$$dev(\%) = \frac{(\gamma^{\mathrm{relax,PBE}} - \gamma^{\mathrm{relax,TPSS}})}{\gamma^{\mathrm{relax,PBE}}} \cdot 100 \qquad \text{(Eq. 42),}$$

and plotted in Figure 10.

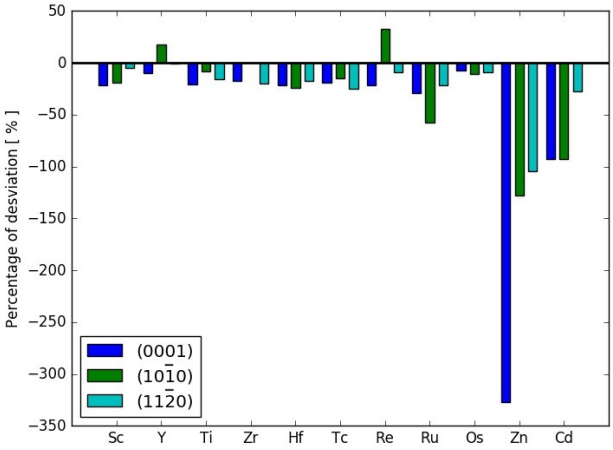

Figure 10. Percentage of deviation between TPSS and PBE for the *hcp* metals under study.

It can be seen that TPSS tend to overvalue surface energies compared to PBE. It is also evident that the description of the d^{10} metals is not very well achieved using TPSS, as the percentage of difference heavily increases, being the functional that is farthest from the experimental data, as it can be proved in Table 6. Note that d^{10} surface energies are the lowest

ones, and due to that, the relative deviation increases for a given absolute error in comparison with the other metals. In addition, the description of their bulk structure using TPSS was also slightly worse than PBE (see Table 1), and since the bulk value energetics is also used in the surface energy calculation, its error is propagated.

There are several reasons why TPSS describes worse metal surfaces than PBE, related with the definition of each functional. GGA functionals, because their self-interaction error, tend to delocalize the electrons of the system, which is not a problem for metallic systems, but it is for molecular calculations, semiconductors, or insulating solids. Hybrid functionals solve this problem by introducing the HF exchange, but as a result, they deliver inaccurate results for metals. Meta-GGA are in between these two types of functionals, and as a result, its results are also with an accuracy between the obtained with the other two.

There is also another factor to take into account, which is the use of PBE pseudopotentials in TPSS calculations. Pseudopotentials are approximations to the description of the core electrons of a given system, which are used in calculations in order to reduce the computational cost of the simulation, describing the core electrons as a non-changing system. This approximation is based on the idea that simulating any process, like the generation of a surface or the adsorption of a molecule, may not affect the internal electrons of an atom, and it will only affect its valence electrons. The values of these pseudopotentials are usually calculated and adjusted for every metal. The possible source of error related with this approximation is that the TPSS calculations were carried out using pseudopotentials obtained by PBE calculations, and so transferability issues may rise.

In addition to the relaxed surface energy, the fix surface energy is calculated in order to study the relaxation energy, defined in Eq 2. Results are plotted in Figure 11. The fix surface energy is always a higher value than the relaxed surface energy, as the energy lowers during relaxation. So, the highest point for each relaxation energy in Figure 11 belongs to the fixed surface energy.

Analyzing the relaxation energies, it can be seen that the metals that have the highest relaxation energies are the ones of groups VII and VIII (Tc, Re, Ru, and Os), and the metals of groups III, IV, and XII (Sc, Y, Ti, Zr, Hf, Zn, Cd) tend to have little relaxation energies. This fact goes in agreement with the inherent stability of each surface. Those metals with the most unstable bulk-truncated surfaces, when they relax, their surface energies decrease more than

those metals with an already highly stable bulk-truncated geometry (in Figure 11, those metals with both fixed and relax surface energies in lower positions are the ones with the shorter straight line).

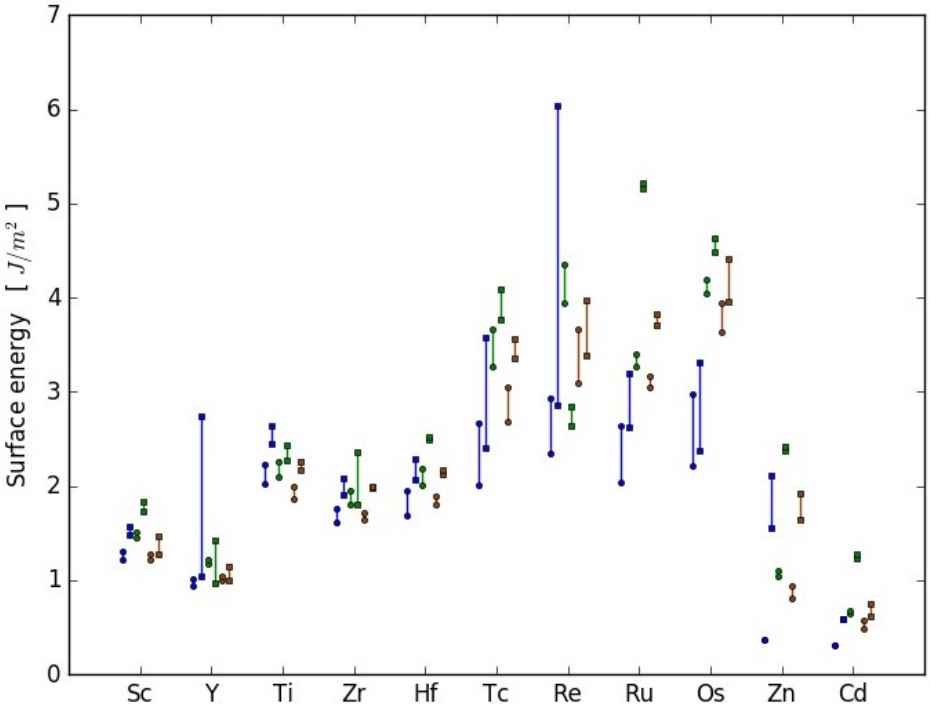

Figure 11. PBE (circles) and TPSS (squares) fix surface energies (highest point), relaxed surface energies (lowest point), and relaxation energy (line between points), for the three surfaces under study (blue for (0001), green for $(10\bar{1}0)$, and brown for $(11\bar{2}0)$).

A study of the trends on relaxed surface energy, see Figures 10 and 11, shows firstly an increase until d^6 metals, and a decrease to d^{10} atoms respect the d^6 ones. This volcano trend has a chemical meaning as is related with the cohesive energy exposed in the bulk section. This is because when the cohesive energy is high, the creation of a surface will also have a higher energetic cost, increasing the surface energy. However, the trend along a group is no maintained, as γ^{relax} does not increase when going down a group. Therefore, surface electronic arrangement must counteract this trend observed in the bulks.

Focusing now in the surface structural relaxation, the geometrical relaxation between layers has been calculated and expressed as a percentage of the relaxed distance, as tipically described from Low Energy Electron Diffraction (*LEED*) experiments. See Figure 12 to get a visual idea of the meaning of the interlayer relaxation, which is the difference between the interlayer distance in the fixed and relaxed systems.

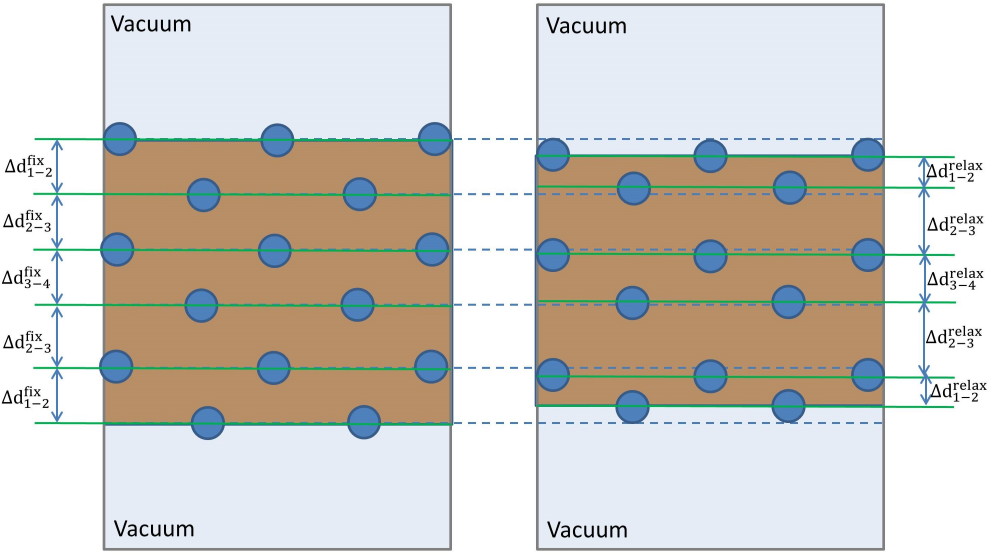

Figure 12. Scheme of the interlayer relaxation. Left, fixed structure, and right; relaxed structure.

In Figure 12 one sees one of the possible relaxation patterns, where the firsts layers are compressed as a result of the creation of the surface strengthening the bond with the bulk, and then the distance between the second and third layer is expanded because of this first compression. The surface creation should affect less at the internal layers, and more at the surface layers. The structural surface relaxations are plotted in Figures 13, 14, and 15.

For the (0001) surface, the pattern previously exposed is seen in most of the cases, despite d^{10} metals, probably due to their full *d*-band, suffer an increase of the distance between the first two layers, which could be related with a bulk compression, consistent with their weak cohesion. The principal trend observed is, as predicted, a percentage of relaxation higher for the

surface layer than for the other inner layers. Also despite some exceptions, the relaxation at PBE and TPSS level are in concordance.

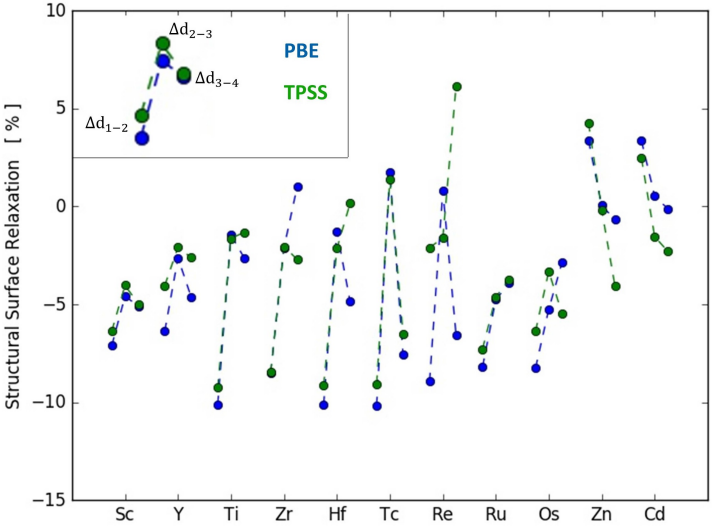

Figure 13. Surface structural relaxation for the (0001) surface.

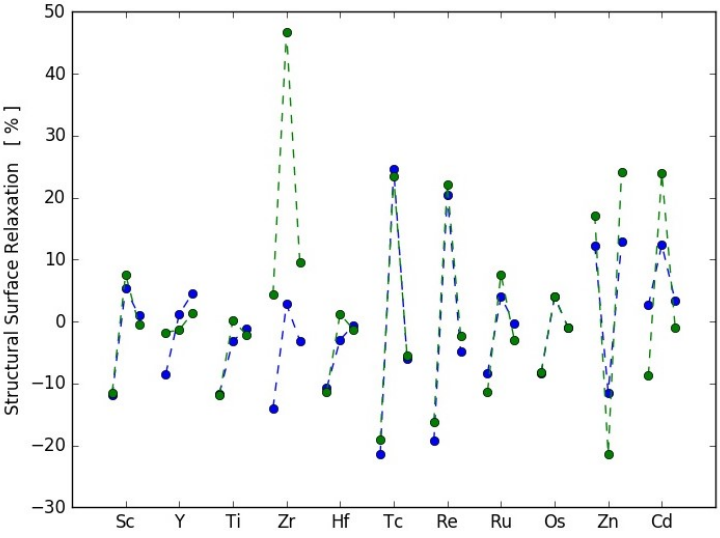

Figure 14. Surface structural relaxation for the $(10\bar{1}0)$ surface.

The surface structural relaxation for the $(10\bar{1}0)$, shown in Figure 14, follows a similar trend that the obtained for the (0001), but with a notorious difference between PBE and TPSS in Zr, and a different pattern in d^{10} metals, where stacking seems to play a role in layer repulsion.

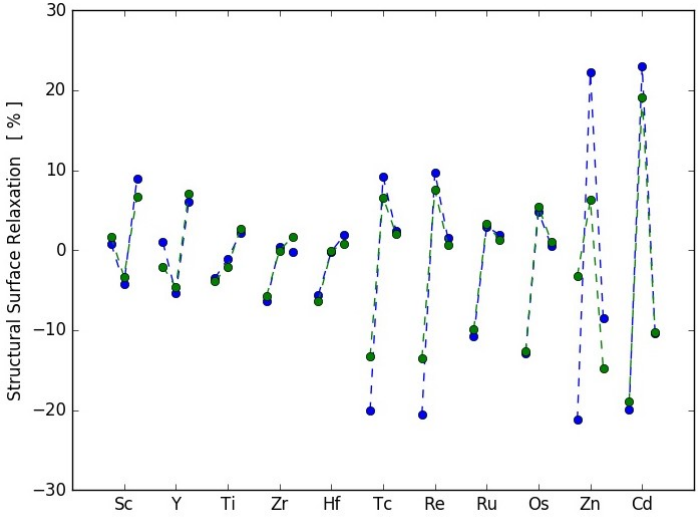

Figure 15. Surface structural relaxation for $(11\bar{2}0)$ surface.

Lastly, the $(11\bar{2}0)$ surface differs a bit for d^1 metals, which feel the contraction in the distance between the second and the third layer. This is a similar situation to the expansion observed in d^{10}. Also a different trend is observed for d^2 metals, which appears also in some isolated cases, where there is only a contraction of the first interlayer distance, and the others expanded.

The experimental data for the interlayer relaxation is very sparse, and only few cases are obtained. For the (0001) Scandium surface, a -2% of relaxation between the first and the second layer is reported,[21] which is in concordance with the -7% contraction here calculated. Also, for $(10\bar{1}0)$ surface, an interlayer relaxation for the two firsts layers of -17% for Re and of -6% for Ti is reported,[22] values that are also in agreement with the ones plotted in Figure 14.

At this point, all the surface properties are shown and described. Next, the electronic descriptors are studied.

7.3. CHEMICAL DESCRIPTORS

Before starting the study of the results obtained for the chemical descriptors, which are the *d*-band center (ε_d), the width corrected *d*-band center (ε_d^W), and the maximum point of the Hilbert transform of the *d*-band (ε_u), let us first study the appearance of the *d*-band as well as the Hilbert transform.

The *d*-band of an atom expresses the contribution of this atom to the total metal band, and an example of it can be seen in Figure 16 for Ru bulk. The *d*-band center stablishes the gravimetric center of the graph observed, which for this case is -1.47 eV.

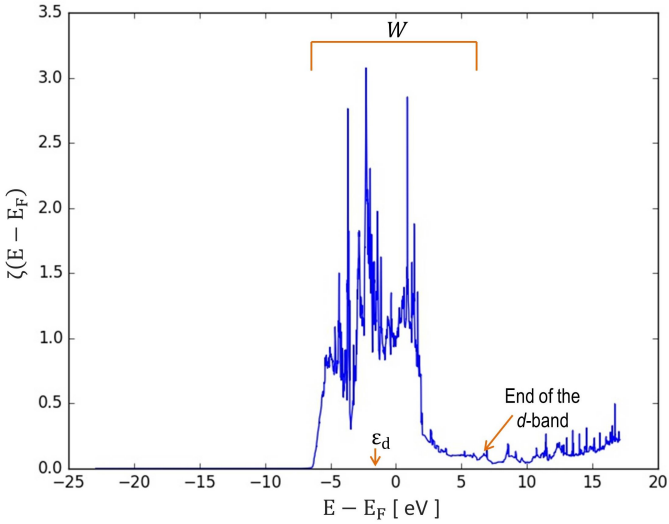

Figure 16. *d*-band diagram for Ru bulk at PBE level.

The width corrected *d*-band center introduces the correction of the *d*-band width, which is not considered in the *d*-band center. Notice that the *d*-band has no end, so an end point must be estimated as the energy where the integral of the graph corresponds to a d^{10} structure.

Finally, the maximum point of the Hilbert transform of the *d*-band comes from the application of the Hilbert transform to the previous function and taking only the imaginary part, see the corresponding characteristic form shown in Figure 17.

The value for this descriptor is the energy of the maximum point. There is no background further chemical meaning in the application of this transform, and this descriptor was proposed only because of an empirical evidence of its possible utility.[10]

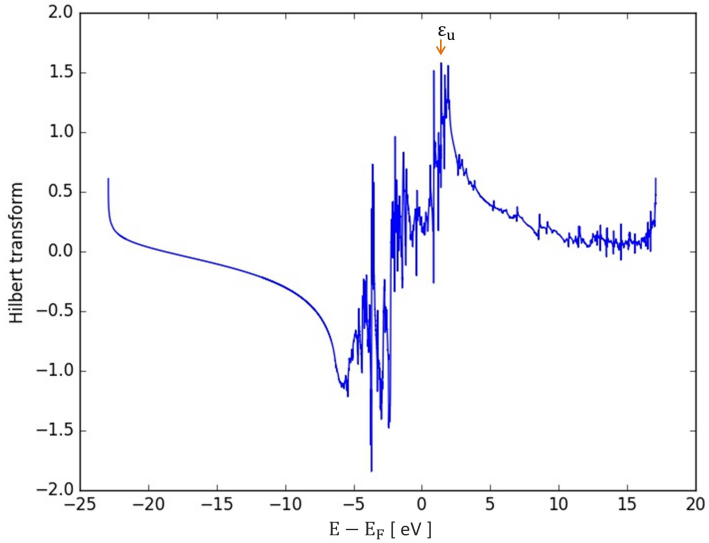

Figure 17. *d*-band Hilbert transform for Ru bulk at PBE level.

As exposed in computational details, these descriptors were obtained using an own written program. In order to test the program as well as the calculations methodology, some *hcp* bulks were chosen and the descriptors obtained values are compared with values reported in the literature at PBE level. Note that in Table 7 ε_d^W does not appear, but appears W as the witdh of the *d*-band.

	Bulk descriptors [eV]					
	PBE			**Prev.[23]**		
	ε_d	W	ε_u	ε_d	W	ε_u
Sc	4.02	21.90	3.93	4.18	20.91	3.93
Hf	3.23	19.11	6.41	3.07	15.97	6.73
Re	0.86	25.77	4.20	1.02	23.76	4.35
Os	-0.50	26.53	2.58	-0.80	22.43	2.41
Cd	-8.91	9.81	-8.41	-9.16	9.76	-8.21

Table 7. Calculated bulk descriptors using the own written program compared with previous calculations.

It can be seen that the values obtained are in clear agreement with the reported values from previous calculations for the two descriptors and the *d*-band width. So, the program is suited to be used in surface calculations.

The obtained *d*-band centers for the three surfaces under study are shown in Table 8.

	ε_d [eV]					
	PBE			TPSS		
	(0001)	$(10\bar{1}0)$	$(11\bar{2}0)$	(0001)	$(10\bar{1}0)$	$(11\bar{2}0)$
Sc	4.53	3.48	2.96	3.51	3.04	2.94
Y	4.21	3.18	2.77	2.53	2.64	2.53
Ti	3.42	3.35	2.58	3.76	3.52	2.85
Zr	3.28	3.25	2.60	3.00	3.41	2.06
Hf	3.27	2.80	2.23	4.31	3.72	2.73
Tc	-0.55	-0.58	-0.81	-0.54	-0.63	-0.77
Re	1.22	1.04	0.80	1.08	1.28	1.08
Ru	-1.48	-1.14	-1.28	-1.51	-1.23	-1.32
Os	-0.20	0.12	-0.11	-0.03	0.08	-0.02
Zn	-7.19	-6.76	-7.13	-7.67	-7.22	-7.58
Cd	-8.75	-8.36	-8.58	-7.49	-7.17	-7.44

Table 8. Calculated surface *d*-band center at PBE and TPSS level for the three surfaces under study.

In order to check the concordance between PBE and TPSS results and study the possible trends of ε_d, the obtained values are ordered in Figure 18 following their series order.

The first trend observed is a decrease of the values along a series. Note that d^n expresses the position in the periodic table, but not the *d* occupancy, where sometimes (Ru and Tc) a $s^1 d^{n-1}$ occupation is found. Notice that because of the lack of d^3, d^4, d^8, and d^9 hcp metals, the abrupt decrease observed have to be taken with caution, and an equally spaced distribution would lead to a smooth decrease.

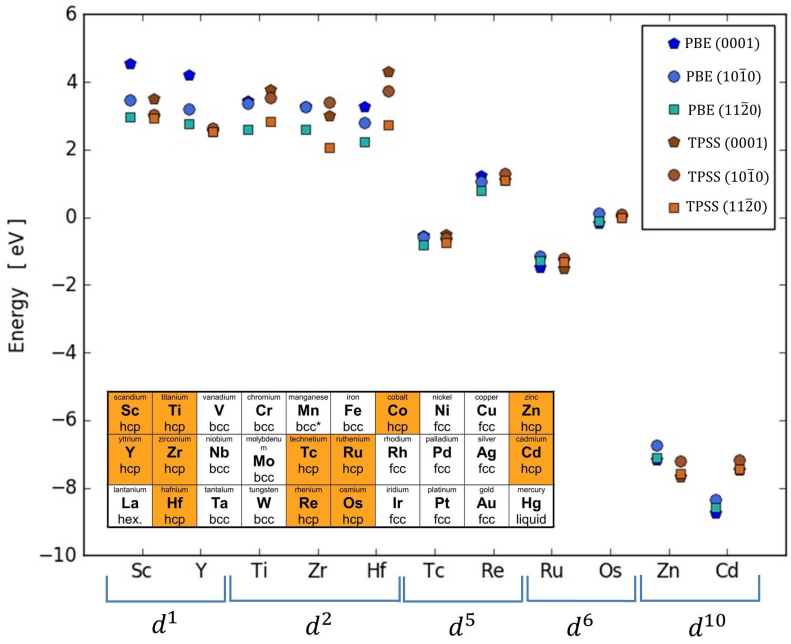

Figure 18. Evolution of ε_d with the occupation of the *d*-band for the studied transition metals.

If ε_d follows a concordance with the metallic surfaces reactivity, its value should be higher if the reactivity of a surface is higher. Following this rule, the most active metal surfaces will be the first ones of early transition metals, and the less active the last ones. This trend agrees with the stablished series trends, where those metals with higher *d*-band occupancy (Au, Ag) are called noble metals due to their low activity, plus the known high activity of early transition metals. So, these trends are followed by ε_d. The group trend obtained on cohesive energies is only seen on d^5 and d^6 metals, where the change is noticeable. Notice that ε_d values increase from bulk values in Table 7, meaning that surfaces, as natural, are more active than bulk.

Focusing in the difference between PBE and TPSS values, a really similar description for both functionals is found. The agreement on electronic properties obtained from surface calculations is clearly better in ε_d than for γ^{relax}, see Figure 11 and 18. So, ε_d estimations are less affected for the choice of functional than surface energies.

Last, one can study which of the three studied surfaces is more active. One would expect that most stable surfaces would be the less active. However, if ε_d describes well the difference between surfaces, the most reactant surface would be (0001) for early transition metals, and

$(10\bar{1}0)$ in the lasts. The differences between the values obtained for each surface are very little, and the *d*-band includes only indirect information about the surface created. So, it cannot be concluded if the ε_d or any of the electronic structure based descriptors allow comparing the reactivity between different surface endings for a given metal.

The next studied descriptor is the width corrected *d*-band center, ε_d^W, whose obtained values are listed in Table 9.

ε_d^W [eV]						
	PBE			TPSS		
	(0001)	$(10\bar{1}0)$	$(11\bar{2}0)$	(0001)	$(10\bar{1}0)$	$(11\bar{2}0)$
Sc	16.90	14.28	12.51	14.22	12.65	12.11
Y	13.62	11.00	9.52	8.16	8.02	8.16
Ti	15.80	15.83	13.62	17.05	16.46	14.68
Zr	13.04	13.22	11.43	12.04	12.63	9.24
Hf	13.18	11.92	9.97	17.21	15.66	12.62
Tc	6.39	6.27	5.53	6.31	5.67	5.31
Re	14.61	14.25	13.70	13.77	13.89	13.77
Ru	4.99	5.47	4.90	4.91	5.63	4.89
Os	13.54	13.55	13.00	13.17	13.34	13.15
Zn	-2.06	-1.74	-2.31	-2.03	-1.12	-2.11
Cd	-3.89	-3.58	-3.86	-2.91	-2.34	-2.89

Table 9. Calculated surface width corrected *d*-band center at PBE and TPSS level for the three surfaces under study.

The obtained values are analyzed checking if the trends observed in ε_d are also here present. In Figure 19 a similar trend can be seen. The most active metals are the earliest, but with a higher differentiation between the values obtained for each surface for d^1 and d^2 metals. Also the trend down a group seems the inverse of the expected, as the descriptor value decreases.

The values obtained at PBE and at TPSS level differs here quite more than what differed for ε_d descriptor, clearly linked to some higher differences on the width of the *d*-band.

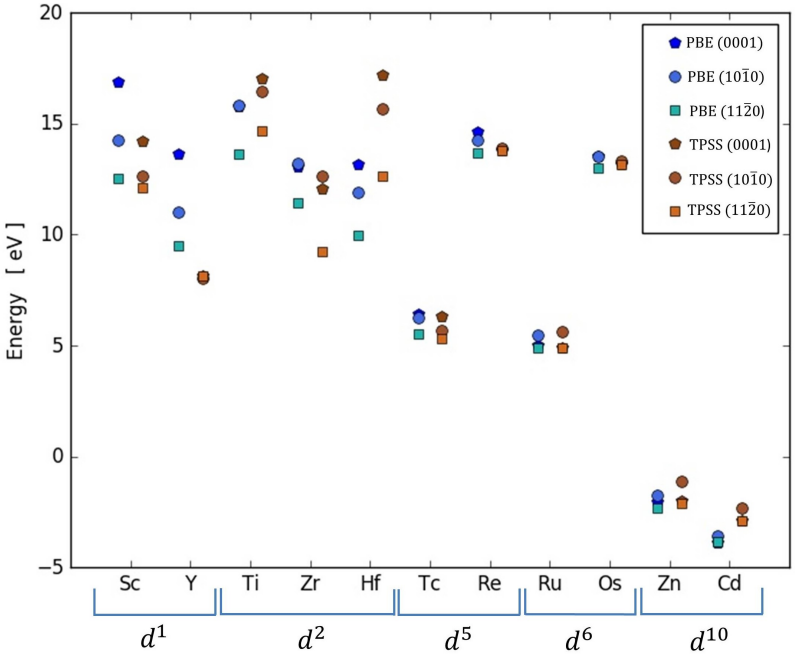

Figure 19. Evolution of ε_d^W with the occupation of the *d*-band for the studied transition metals.

The differences in ε_d^W and ε_d trends are incorporated by the *d*-band width, so to analyze how changes for the metals under study, it is plotted in Figure 20, which shows a larger differentiation between surfaces than in ε_d. This goes in the same way as observed in Figure 18 for ε_d, but just increasing the differences. So, if the most stable surface is the most reactant, this descriptor introduces some information about the surface geometry, as the *d*-band width seems to change with the CN of the surface. However, the difference between PBE and TPSS values for each descriptor increases, producing more dispersion of results.

Another trend observed is a larger decrease of *W* while going down a group for d^1 and d^2 metals. Lacking a comparison with adsorption simulations, see below, it seems that *W* does not introduce any improvement to ε_d as changes along groups or series do not follow the supposed activity pattern.

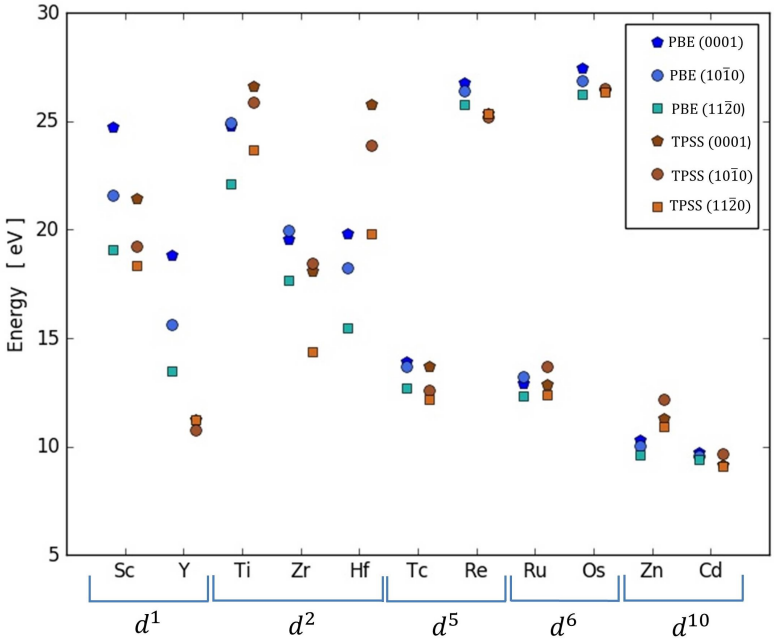

Figure 20. Evolution of W with the occupation of the *d*-band for the studied transition metals.

The last descriptor under study is the maximum point of Hilbert transform of the *d*-band, ε_u, which, as exposed previously, does not have any further physicochemical reason which explains its definition, and just posed on an empirical concordance. The obtained values for ε_u are shown in Table 10.

ε_u [eV]						
	PBE			TPSS		
	(0001)	(10$\bar{1}$0)	(11$\bar{2}$0)	(0001)	(10$\bar{1}$0)	(11$\bar{2}$0)
Sc	3.12	2.47	2.43	-0.03	2.46	2.58
Y	5.24	3.62	2.93	4.44	1.19	4.44
Ti	3.69	2.52	2.09	3.79	2.28	1.79
Zr	2.61	3.45	2.83	5.12	5.57	4.51
Hf	6.26	0.99	3.32	5.97	3.66	3.25

Tc	-0.47	1.26	2.96	2.95	1.76	1.32
Re	3.57	1.10	2.82	-4.17	2.55	-4.17
Ru	1.41	0.65	1.22	1.46	0.91	0.15
Os	2.34	1.38	0.71	-2.59	2.25	1.30
Zn	-6.94	-6.47	-6.69	-7.36	-6.87	-7.21
Cd	-8.47	-7.99	-8.10	-6.73	-6.60	-6.84

Table 10. Calculated surface maximum point of the imaginary part of the Hilbert transform of the *d*-band at PBE and TPSS level for the three surfaces under study.

As done for the other descriptors, the study of the trends are shown in front of the occupancy of the *d*-band, see Figure 21.

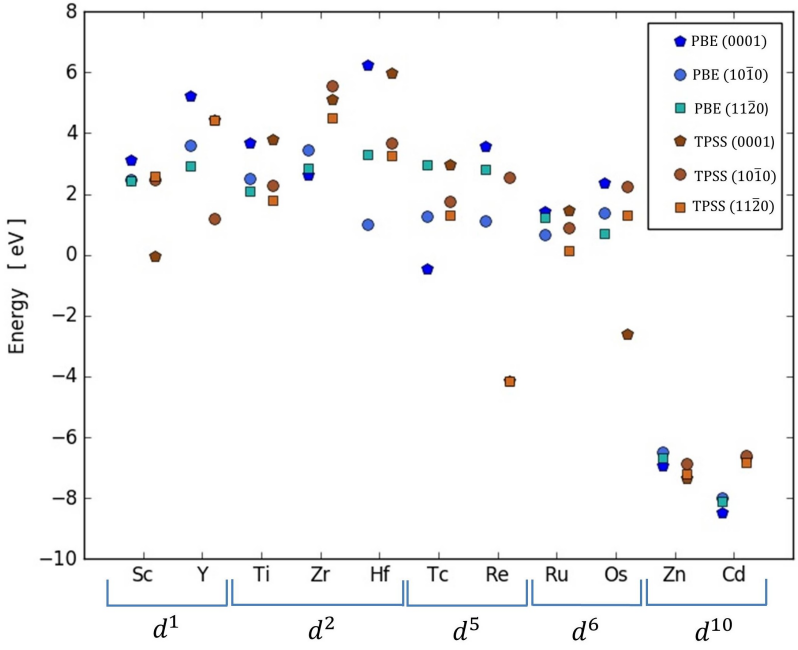

Figure 21. Evolution of ε_u with the occupation of the *d*-band for the studied transition metals.

The evolution along the periodic table of this descriptor shows the same trend as the other ones, decreasing while the *d*-band is being filled. These tends to support its usage. However, the dispersion of values is much higher than it was for ε_d, and does not seem to follow any

trend while going down a group. Also the description for PBE and TPSS differs more than did for ε_d. Comparing between surfaces, (0001) is for early transition metals the one with a higher value, as found for other descriptors, but from d^5 and d^6 there is no clear pattern, with discrepancies between PBE and TPSS most reactive surface. Therefore, despite the general good trend, this descriptor seems to work worse than ε_d, and its usage as a substitute cannot be justified with the obtained results.

At this point, all the descriptors under study are obtained and analyzed in front of general trends, but the best way to check the good concordance of the descriptors with an adsorption process on its surface is directly comparing with adsorption values, previously calculated. See in Table 11 calculated H atom adsorption energies on a hollow site of (0001) surface, where a lower value indicates a stronger bonding.

Sc	**Ti**	**V**	**Cr**	**Mn**	**Fe**	**Co**	**Ni**	**Cu**	**Zn**
-0.92	**-0.99**	**-0.88**	**-0.69**	**-**	**-0.54**	**-0.31**	**-0.37**	**0.07**	**-**
Y	**Zr**	**Nb**	**Mo**	**Tc**	**Ru**	**Rh**	**Pd**	**Ag**	**Cd**
-0.92	**-0.91**	**-0.90**	**-0.66**	**-**	**-0.41**	**-0.33**	**-0.42**	**0.42**	**-**
La	**Hf**	**Ta**	**W**	**Re**	**Os**	**Ir**	**Pt**	**Au**	**Hg**
-	**-**	**-0.90**	**-0.61**	**-0.65**	**-**	**-0.24**	**-0.37**	**0.33**	

Table 11. H adsorption energies (in eV) on (0001) surface hollows.[24]

With these H adsorption energies, global trends can be treated. Notice that not all metals reported have the same stacking pattern, so, as exposed in Figure 1, some of them are *hcp*, but others *bcc* or *fcc*. The general trend is that the most reactant metals are those located at the left, and then the activity decreases while *d*-band is filled. This is in agreement with the previously exposed trends.

The lowering of a group seems to imply a decrease of the activity in general, but missing values do not allow confirming a general trend, as the changes in adsorption energies are small. Keeping in mind that the descriptors must follow the inverse trend of the adsorption energy, one can discuss which descriptor is better, despite having values only for six of the twelve *hcp* transition metals studied.

The obtained results for ε_d agree very well with the adsorption energies. The d^1 and d^2 groups give similar energies, but there is a decrease for the d^5, d^6, and d^{10} as they are less

active. The description is not better for the other descriptors. First of all, the changes produced for the width correction do not follow the adsorption trend, as they suggest that the reactivity for Os and Re should be similar to the d^1 and d^2 ones, and it is not. Also ε_d^W suggests bigger changes between the same group d^1 and d^2 metals, and this is not observed. So, it can be concluded that at least for the obtained results, the width corrected *d*-band center describes worse the activity trends that the *d*-band center does.

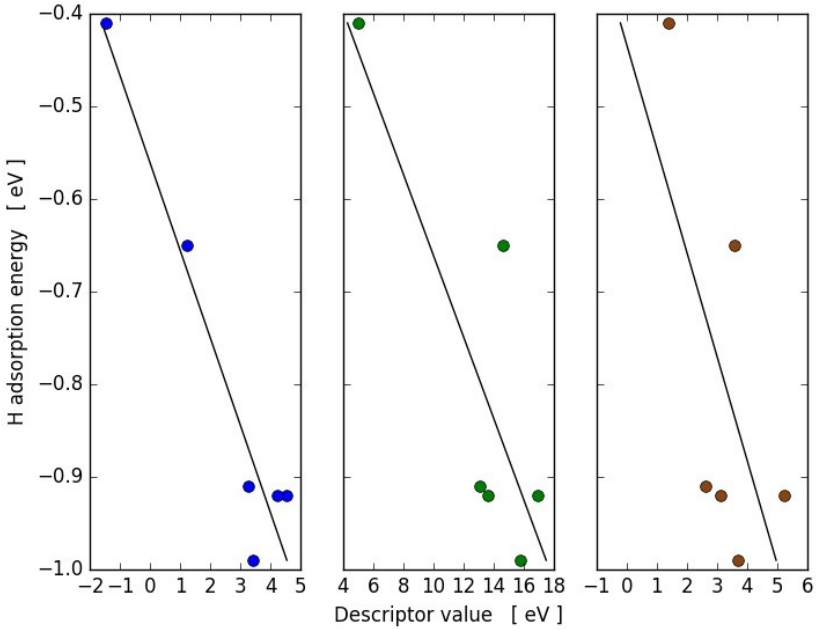

Figure 22. H adsorption energy *versus* the value of the descriptors studied. In blue ε_d, in green ε_d^W, and in brown ε_u.

Finally, ε_u dispersion is not expressed in H adsorption energies, and it does not describe well the decrease in these values for the d^5 and d^6 metals. In fact, the only evidence well described with this descriptor is the decrease of the reactivity for d^{10} metals. So, it can be also affirmed that this empirical descriptor does not explain the reactivity of *hcp* metals, and because of that, does not introduces well as a descriptor at least for these systems.

8. CONCLUSIONS

In summary, the following points can be concluded out of the obtained results:

- Both PBE and TPSS deliver a good description of bulk properties for the studied *hcp* transition metals, particularly on cohesive energies and shortest interatomic distances.

- Surface energies are better described at PBE than at TPSS level.

- The most stable surface is the (0001), followed by the $(11\bar{2}0)$, and letting as the less stable be the $(10\bar{1}0)$; this order does not follow their CN.

- The *d*-band center trends for *hcp* transition metals are in concordance with the activity of their surfaces as shown for H adsorption on (0001) surfaces.

- The width correction to the *d*-band center does not introduce any improvement to the *d*-band center, as provides a worse description of the activity.

- The maximum point of the Hilbert transform of the *d*-band only describes the lower activity of d^{10} metals, and with the present calculations cannot be reaffirmed as a good chemical descriptor.

9. REFERENCES AND NOTES

1. Van Santen, R.: Future prespectives in catalysis. *NRSC-Catalysis* **2009**, 4, 1-84.
2. Erisman, J.; Suttor, M.; Galloway, J.: How ammonia changes the world. *Nat. Geos.* **2008**, 10, 636-639.
3. Nørskov, J. K.; Bligaard, T.; Christesen. C.H.: Towards the computational design of solid catalysts. *Nat. Chem.* **2009**, 1, 37-46.
4. Van Houten, J.: A Century of Chemical Dynamics Traced through the Nobel Prizes. 1909: Wilhelm Ostwald. *J. Chem. Educ.* **2002**, 79, 146-148.
5. Mariño, F.; Boveri, M.; Baronetti, G.; Laborde, M.: Hydrogen production from steam reforming. *Int. J. Hydrogen Energy* **2001**, 26, 665–668.
6. Perdew, J.; Burke, K.; Ernzerhof M.: Generalized Gradient Approximation Made Simple. *Phys. Rev. Lett.* **1997**, 78, 1396.
7. Tao, J.; Perdew, J.; Staroverov, V. N.; Scuseria, G. E.: Climbing the density functional ladder: nonempirical meta-generalized gradient approximation designed for molecules and solids. *Phys. Rev. Lett.* **2003**, 91, 3865-3868.
8. Bligaard, T.; Nørskov, J. K.: Ligand effects in heterogeneous catalysis and electrochemistry. *Electrochim. Acta* **2007**, 52, 5512–5516.
9. Vojvodic, A.; Nørskov, J. K.; Abild-Pedersen F.: Electronic Structure Effects in Transition Metal Surface Chemistry. *Top. Catal*. **2014**, 57, 25–32.
10. Xin, H.; Vojvodic, A.; Voss, J.; Nørskov, J. K.; Abild-Pedersen F.: Effects of d-band shape on the surface reactivity of transition-metal alloys. *Phys. Rev. B* **2014**, 89, 115114.
11. Paniagua, J.C; Alemany, P.: *Química quàntica (2),* 1st ed.; Llibres de l'índex: Barcelona, 2000.
12. Becke, A. D.. Density-functional thermochemistry. III. The role of exact Exchange. *J. Chem. Phys.* **1993**, 98, 5648−5652.
13. Paier, J., Marsman, M.: Why does the B3LYP hybrid functional fail for metals?. *J. Chem. Phys.* **2007**, 127, 024103.
14. Kittel, C.: *Introduction to Solid State Physics,*1st ed.; Willey: New York, 1998.
15. Kresse, G.; Furthmuller,: Efficient iterative schemes for ab initio total-energy calculations using a plane-wave basis set. *Phys. Rev. B* **1996**, 54, 11169−11186.
16. Blöchl, P. E.: Projector augmented-wave method. *Phys. Rev. B* **1994**, 50, 17953-17979.
17. Patanachai, J.; Kozlov, S. M.; Viñes, F.; Limtrakul, J.; Illas, F.: Establishing the Accuracy of Broadly Used Density Functionals in Describing Bulk Properties of Transition Metals. *J. Chem. Theory Comput.* **2013**, 9, 1631–1640.

18. Patanachai, J.; Luo, S.; Kozlov, S. M.; Viñes, F.; Limtrakul, J.; Truhlar, D. G.; Illas, F.: Bulk Properties of Transition Metals: A Challenge for the Design of Universal Density Functionals. *J. Chem. Theory Comput.* **2014**, 10, 3832−3839.
19. Vitos, L.; Ruban, A.V.; Skriver, H.L.; Kollar. J.: The surface energy of metals. *Surf. Sci.* **1998**, 411, 186–202.
20. Ruvireta, J.; Vega, L.; Viñes, F.: Cohesion and Coordination Effects on Transition Metal Surface Energies. *Surf. Sci.* **2017**, 664, 45–49.
21. Tougaard, S.; Ignatiev, A.; Atomic structure of the Scandium (0001) Surface. Surf. Sci. **1982**, 115, 270-278.
22. Barnett. S.D.: Angle-resolved Photoemission and LEED from rare-earth metals. *Surf. Sci. Rep.* **1992**, 14, 271-354.
23. Notario-Estevez, A.; Kozlov, S. M.; Viñes, F.; Illas F.: Electronic-structure-based material descriptors: (in)dependence on self-interaction and Hartree–Fock exchange. *Chem. Commun*. **2015**, 51, 5602-5605.
24. Kristinsdóttir, L.; Skúlason, E.: A systematic DFT study of hydrogen diffusion on transition metal surfaces. *Surf. Sci.* **2012**, 606, 1400–1404.

10. ACRONYMS

bcc – Body centered cubic

B3LYP – 3-parameter, Becke-Lee-Yang-Parr

CN – Coordination number

DFT – Density functional theory

DOS – Density of states

fcc – Face centered cubic

GGA – General gradient approximation

hcp – Hexagonal close packed

HF – Hartree Fock

HOMO – Highest occupied molecular orbital

KS – Kohn-Sham

LDA – Local density approximation

MAPE – Mean absolute percentage error

MPE – Mean percentage error

PAW – Projector augmented wave

PBE – Perdew-Burke-Ernzerhof

TPSS – Tao-Perdew-Staroverov-Scuseria

VASP – Vienna *ab initio* simulation package

xc – Exchange correlation